Multiscale characterization of effective thermal properties of graphene/polymer composite aerogels

D.-T. Le, V.-H. Nguyen, S. Mahouche-Chergui, B. Carbonnier, Daniel Grande, S. Naili

Multiscale characterization of effective thermal properties of graphene/polymer composite aerogels

D.-T. Le[a,b], V.-H. Nguyen[a], S. Mahouche-Chergui[b], B. Carbonnier[b], D. Grande[b,c], S. Naili[a,*]

[a] *Univ Paris Est Creteil, Univ Gustave Eiffel, CNRS, UMR 8208, MSME, F-94010 Créteil, France*
[b] *Univ Paris Est Creteil, CNRS, ICMPE, UMR 7182, 2 rue Henri Dunant, 94320 Thiais, France*
[c] *Present address: Univeristy of Strasbourg, CNRS, ICS, UPR 22, 23 rue du Loess, 67034 Strasbourg, France*

Abstract

This work involves the characterization of effective thermal conductivity of polymer aerogel reinforced by graphene and graphene oxide elaborated by replacing the liquid phase with a gas phase through an environmentally friendly freeze-drying process. For characterizing the developed aerogel, multiscale geometrical configurations were constructed based on the experimental characterizations of the prepared aerogels. Following that, a homogenization procedure was applied, moving from smaller to larger scales. At the nanoscale, the Milton method was used, while at the micro- and macroscales, the asymptotic method was employed in combination with the finite element method. Problems posed on a domain called the representative unit cell were formulated at both micro- and macroscales, and their resolution using the finite element method allows the calculation of characteristic functions of the problems, thereby obtaining effective thermal conductivity of the material. To the best of our knowledge, no studies have been reported in the literature on the multiscale characterization of the effective properties of polymer aerogels, hence the motivation for this work. To address this gap, a novel numerical approach has been developed to investigate aerogel properties across multiple scales. The multiscale approaches have revealed the influence of various microstructural characteristics on the effective thermal conductivity properties of the hybrid aerogel. The results show that graphene and graphene oxide nanoinclusions do not significantly affect the thermal conductivity, but they do significantly improve the mechanical properties of the polymer-based aerogel. Furthermore, this study has also demonstrated that aerogels with superinsulating properties can be obtained by reducing the pore size to the nanometer scale and lowering the gas pressure to below 0.01 atm.

Keywords: Asymptotic homogenization, effective thermal properties, finite element method, composite aerogel, graphene, biopolymer

1. Introduction

The continuous increase in global energy consumption has always been a major concern for decades. Buildings were the most consuming sector, accounting for approximately a third of global energy consumption [1] and even as much as 41% of the total energy consumption in Europe [2].

*Corresponding author
Email address: naili@u-pec.fr (S. Naili)

Hence, reducing energy consumption in buildings through the use of insulation materials is considered as one of the solutions to this issue, simultaneously contributing to maintaining human comfort in daily lives. It should be noted that materials without high thermal insulation performance will require substantial thickness, which can lead to a reduction in living space. Therefore, increasing thermal insulation performance by reducing thermal conductivity will be a crucial objective in the development of insulation materials. Several commonly used insulation materials include polyurethane foam, mineral wool, and vacuum insulation panels (VIP) providing a range of insulation solutions that can be tailored to specific needs. Closed-cell structure of polyurethane foams reduces significantly heat transfer, resulting in excellent thermal resistance required for residential applications. Mineral wool combines thermal insulating properties with fire resistance and soundproofing qualities. VIP offer the highest thermal resistance through vacuum-driven minimization of conductive and convective heat transfer. Additionally, their thin profile allows for exceptionally effective insulation in tight spaces based on factors such as thermal performance, fire safety, moisture resistance, and space limitations. However, these materials still have limitations, such as problems related to aging for VIPs [3]. Therefore, aerogels, known for their extremely low internal thermal conductivity ranging from 0.0034 to 0.022 W/(m·K), have attracted increasingly more attention in the building sector [4]. In recent years, it has been demonstrated that graphene-reinforced polymer composite aerogels are a promising alternative to silica aerogels due to their low cost and improved mechanical properties [5, 6, 7]. Caring for environmental sustainability, abundant natural biopolymers, notably chitosan, was used as a polymer matrix in combination with an environmentally friendly freeze-drying method for the development of aerogels [5, 6]. Indeed, the freeze-drying method offers various advantages, especially cost-effectiveness, due to the direct use of water as a solvent and, the simple drying process through sublimation [8]. We firmly believe that freeze-drying can be regarded as an environmentally friendly process as it operates at low temperatures avoiding the need for high-energy inputs required for supercritical conditions which involves temperatures above 30°C and pressures of 70 bar or more. Additionally, freeze-drying primarily uses water as a solvent, which is abundant, non-toxic, non-flammable, and environmentally benign, producing no hazardous waste as compared to some organic solvents. These factors significantly reduce the environmental impact associated with solvent production, handling, and disposal, unlike the solvent exchanges often used in supercritical drying, such as replacing ethanol or acetone with CO_2.

There are various experimental methods that can be employed to characterize the thermal conductivity of aerogels, such as the transient plane source (TPS) [9], the hot-wire method [10] and the heat flow method [11, 12, 13], etc. However, experimental works are either unfeasible or may require significant efforts when conducting parametric studies related to changes of parameters at the nano- and microscales. Hence, numerical simulations become essential for predicting the effective thermal conductivity of aerogels and simultaneously for optimizing the material manufacturing processes.

In the literature, several analytical methods are often used to predict the thermal conductivity of aerogels, such as the models by Zeng *et al.* [14], Dan *et al.* [15] and Xie *et al.* [16]. The limitations of these models include their inability to flexibly describe the microstructure of aerogels, particularly the complex multiscale structure of nanoinclusion-reinforced polymer composite aerogels. Furthermore, the asymptotic homogenization method allows for predicting the effective thermal conductivity of heterogenous materials based on representative unit cells [17]. This implies that this method allows for the calculation of the effective thermal conductivity of the solid phase, including nanoinclusions (namely fillers), and the polymer matrix at the microscale, as well as the

effective thermal conductivity of the aerogels created by the pores and the solid network at the macroscale. Therefore, the homogenization theory is highly useful for establishing the relationship between parameters at low scales, such as nano- and microscales, and the effective thermal conductivity of aerogels.

Regarding the effects of graphene and its derivatives, namely graphene oxide (GO) and reduced graphene oxide (rGO), it has been reported that these bidimensional materials can significantly enhance the thermal conductivity of polymer-based composite materials [12, 18, 19, 20, 21, 22]. Furthermore, it is known that graphene and graphene oxide sheets dispersed within a polymer matrix form different structures, such as aggregates, intercalated and exfoliated structures, influencing the effective properties of the materials [23, 24, 25]. As far as we know, no studies have hitherto investigate the effect of microstructure on the thermal conductivity of polymer-based aerogels. In the context of graphene and graphene oxide commonly being used to enhance the mechanical properties of polymer-based insulation materials, experimental studies have primarily provided information about the impact of the filler content on the thermal conductivity of the material [26, 27, 5]. However, other parameters such as porosity and microstructure may also change with filler content [27, 25], which can lead to misconceptions regarding the effects of graphene and graphene oxide. Considering the pore size, it is evident that nanometric pores significantly reduce the thermal conductivity of aerogels due to the Knudsen effect. Although aerogels typically consist of both nanometric and micrometric pores with varying volume fractions, previous researches have mainly focused on materials with nanometric pores [28] or with a fixed volume fraction of these pores [29], thus lacking in-depth understanding of the influence of nanometric pores in aerogels. Closely related to the effect of pore size, reducing gas pressure will increase the mean free path of gas molecules, resulting in a decrease in the gas thermal conductivity as this mean free path reaches values in the same order of the pore size. Therefore, the influence of gas pressure on effective thermal conductivity of aerogels needs to be considered in conjunction with the effect of pore size.

The main objective of this study is to perform numerical characterization of the effective thermal conductivity of chitosan aerogels reinforced by graphene or graphene oxide, which were synthesized through the freeze-drying method. The numerical studies will focus on the effect of the microstructural morphology, such as aggregates, intercalated and exfoliated structures, on the effective thermal conductivity of this aerogel, which has not been investigated so far in the literature to date. We are also interested in investigating the influence of pore size and gas pressure on the thermal conductivity of aerogels, taking into account the simultaneous presence of nanometric and micrometric pores with varying volume fractions, which has not been addressed in previous works.

Due to the lack of studies in the literature on the multiscale characterization of the effective properties of polymer aerogels, this work aims to fill this gap. A novel numerical approach has been developed to examine the properties of aerogels at multiple scales, and the key contributions of the paper are as follows:

1. chitosan aerogels incorporating variously structured graphene inclusions, ranging from monolayer to aggregates were elaborated and thoroughly characterized.

2. experimental characterization parameters enabled construction of geometrical configurations at various scales and model validation further supported by literature.

3. it is the first attempt that a multiscale characterization of the effective thermal properties of graphene/polymer-based hybrid aerogels is carried out.

4. we conduct extensive studies on the effect of the microstructural morphology, such as aggregate, intercalated and exfoliated structures, on the effective thermal conductivity of these aerogels.

In order to estimate the effective thermal conductivity of the developed aerogels, multiscale geometrical configurations will be constructed based on the experimental characterization, followed by a homogenization process carried out at each scale, progressively from smaller to larger scales. In this contribution, nanopores refer to pores with size below 100 nm, while micrometric pores are defined as larger pores, above 100 nm, and with typical size from a few micrometers to several hundreds of micrometers in size. The aggregate structure of graphene and the exfoliated and intercalated structures of graphene oxide have been examined. Additionally, the variation in aerogel porosity and the presence of nano-sized pores within the polymer matrix with different volume fractions are also considered in this study. In parallel, the numerical results are also compared to experimental data in the literature to check the validity of the proposed model.

The paper is organized as follows. Section 2 introduces the elaboration method and experimental characterization of the aerogels under investigation. Sections 3 and 4 present the construction of geometrical configuration and homogenization methods at different scales, respectively. The numerical results and a discussion about the thermal conductivity are reported in section 5. In this section, the obtained numerical results are also compared with previous experimental work in the literature. Finally, section 6 summarizes the main conclusion of this work.

2. Material elaboration and characterization

2.1. Materials

Graphene nanoplatelets (G, quality level 100: grade C-750, thickness a few nm, particle size $< 2\mu m$, bulk density $0.2-0.4$ g/cm^3 and surface area 750 m^2/g), chitosan with low molar mass and a deacetylation degree of $75-85\%$ (CS), graphite flakes (particle size < 150 μm), glacial acetic acid, sulphuric acid (H_2SO_4, $\geq 97.0\%$), sodium nitrate ($NaNO_3$, $\geq 99.0\%$), potassium permanganate ($KMnO_4$, $\geq 99.0\%$) and hydrogen peroxide 30% (H_2O_2) were purchased from Sigma-Aldrich and used without further purification. Graphene oxide (GO) was prepared starting from natural graphite using Hummers' method [30].

2.2. Instruments used in the tests

The aerogels were characterized using X-ray Diffraction (XRD), Scanning and Transmission Electron Microscopy (SEM, TEM). XRD measurements were performed on a Bruker D8 Advance diffractometer equipped with a Cu Kα source ($\lambda = 1.5418$ Å), operating at 45 kV and 44 mA. Diffractograms were recorded from thin aerogel disks, scanned at a rate of 0.2° per minute across a 2θ range of 5° to 60°. The interlayer distance (d-spacing) of graphene was calculated using Bragg's equation:

$$n\,\lambda = 2d\sin\theta,$$

where $n = 1$ and θ is the diffraction angle.

TEM analysis was carried out on a FEI Tecnai F20 electron microscope at an accelerating voltage of 200 kV. The samples were prepared by dispersing the aerogels in absolute ethanol through ultrasonication, followed by drop-casting the suspension onto copper grids coated with a Formvar-carbon film. SEM analysis was carried out using a Zeiss Merlin microscope (Carl Zeiss, Germany)

equipped with an SE2 detector and operated at 10 kV. Prior to SEM analysis, the aerogels were sectioned with a razor, thoroughly dried, and coated with a 5 nm thin layer of Pd to enhance conductivity. Pore sizes were measured using ImageJ software and addressed in two perpendicular directions for each pore. A total of 30 pores were analyzed per SEM image, with a minimum of 10 SEM images evaluated.

To assess the mechanical properties, uniaxial compression tests were performed using a universal testing machine (Instron model 5567, Boston, Massachusetts, USA) equipped with a 2 kN load cell. Cylindrical aerogel samples (diameter $\sim$ 30 mm, height $\sim$ 20 mm) were compressed to 70% of their original height and then unloaded at 0.5 mm/min.

2.3. Elaboration method

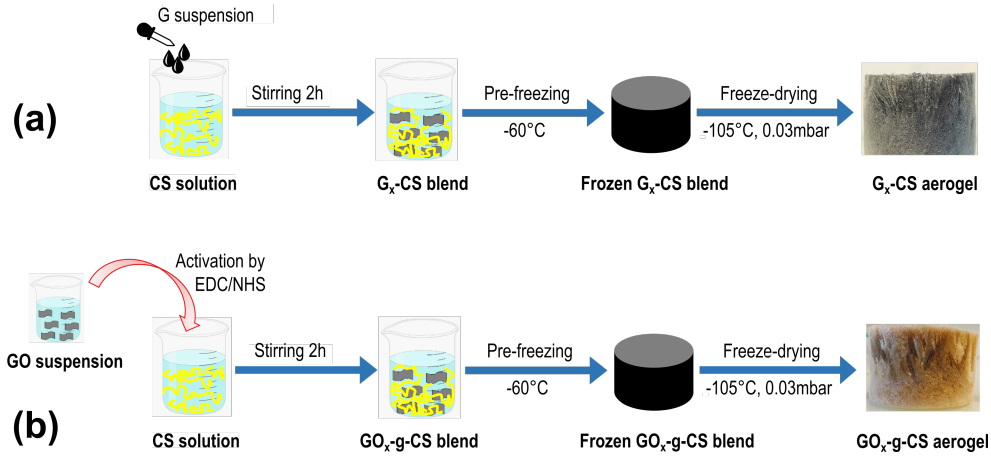

Figure 1: Schematic fabrication diagram of (a) G_x-CS and (b) CS_g-GO_x aerogels using the freeze-drying method.

The studied hybrid aerogels based on biopolymer (chitosan) and nanoinclusions (graphene or graphene oxide) were prepared through an environmentally friendly freeze-drying process. The aerogels' preparation process involved three main steps, including dispersing the nanoinclusions in the polymer matrix to form a homogeneous solution, freezing the sample and finally drying the sample by replacing the liquid phase with a gas phase. In order to prevent the skeleton from collapsing during the drying process, freeze-drying allows us to convert water from the solid phase to a gas phase (sublimation) in a low-temperature and low-pressure environment while keeping the shape of the skeleton intact [31]. The graphene-chitosan composite aerogels, denoted by G_x-CS aerogels with x% representing the percentage by weight of graphene relative to chitosan, were prepared based on previously reported methods [22], as shown in Fig. 1a. Typically, the chitosan solution was prepared by dissolving 2.4 g of chitosan powder in 100 mL of acetic acid aqueous solution (1% v/v). Then, the homogeneous graphene suspension with a desired amount of graphene nanoinclusions (x% weight ratio with respect to the amount of chitosan), as prepared through ultrasonic treatment was added to the chitosan solution.

The mixture was then vigorously stirred for 2 h. The homogeneous mixture obtained was then poured into molds and pre-frozen at -60 °C for 24 h in a temperature-controlled freezer. Finally, the sample was completely dried by freeze-drying after 48 h.

For chitosan grafted graphene oxide aerogel, denoted by GO_x-g-CS with x% representing the percentage by weight of graphene oxide relative to chitosan, the synthesis process is similar to

that of graphene-chitosan aerogel. However, the graphene oxide suspension was activated using the 1-(3-Dimethylaminopropyl)-3-ethyl-carbodiimide hydrochloride (EDC) and N-hydroxysuccinimide (NHS) coupling agents before being added to the chitosan solution (see Fig. 1b).

The grafted aerogels were soaked in a mixture of ethanol/water with a ratio of 9/1 under ultrasonic treatment to remove excess of EDC/NHS, then freeze-dried for 48 hours to complete the process. Moreover, 1-(3-Dimethylaminopropyl)-3-ethylcarbodiimide Hydrochloride (EDC, purity > 98%), N-Hydroxysuccinimide (NHS, purity > 98%) were obtained from TCI. Ethanol was purchased from Alfa-Aesar.

2.4. Experimental characterization

To predict the arrangement of graphene and graphene oxide sheets in the chitosan matrix, X-ray diffraction (XRD) analysis was used. According to the XRD results (see Fig. 2a), the original graphene and graphene oxide powder exhibited a typical diffraction peaks at 26.6° and 11.3° that corresponded to interlayer spacing of 0.335 nm and 0.780 nm, respectively. In the G_{10}-CS aerogel, a weak peak at 26.3° demonstrates the presence of graphene with an interlayer spacing of 0.338 nm. The graphene interlayer distance was almost constant indicating that graphene sheets existed as aggregates in polymer matrix. In contrast, the XRD pattern of GO_{10}-g-CS aerogel did not show any peak of GO indicating that the graphene oxide sheets were highly exfoliated. To determine the number of layers in the aggregates, transmission electron microscopy (TEM) technique was carried out on the G_{10}-CS aerogel sample. The TEM images (see Fig. 2b-c) showed that graphene sheets form aggregates in which the graphene sheets were arranged parallel to each other. There were $4-12$ layers in each assembly with interlayer spacing ranging between 0.33 and 0.35 nm, which coincided with the results obtained from the XRD analysis above. In addition, these aggregates were randomly distributed in the chitosan matrix with a length varying from 30 to 90 nm.

In fact, although graphene oxide was easily dispersed into single sheets (exfoliated structure) in the polymer matrix due to its surface functionality [23], the intercalated structure of graphene oxide had been obtained in some cases. In the work of Blanton *et al.* [24], the distance between two graphene oxide sheets in composites with various polymers and different polymer content were valid in the range of $1.5-5.3$ nm. Therefore, to expand the scope of our research, two types (intercalated and exfoliated) of graphene oxide structures were also considered.

The pore features were preliminarily characterized through scanning electron microscopy (SEM) analysis. SEM images were processed using ImageJ software to determine the pore size. An average of 10 SEM images was considered for each analyzed sample resulting in a total number of pores for determining the pore size of the materials of 300. The pore size was measured twice in two perpendicular directions for each pore. According to the SEM micrographs (see Fig. 3), a three-dimensional structure composed of a network of thin alveolus can be found in both types of aerogels. The alveolus form interconnected pores with average diameters ranging from several tens of micrometers to several hundreds of micrometers. The average diameter of the pores in G_{10}-CS aerogel was approximately equal to 76 μm. Besides, the interconnection of pores was characterized by a void with an average diameter of 12 μm in both aerogels. The obtained structures of our aerogels closely resemble those of aerogels synthesized using freeze-drying methods in previous works [5, 6].

Mechanical tests of graphene-chitosan and graphene oxide-grafted chitosan aerogels were conducted using a universal testing machine at room temperature (Instron 5567, Boston, Massachusetts, America). The samples were cylinder-shaped with a diameter of 30 mm and a height of 20 mm.

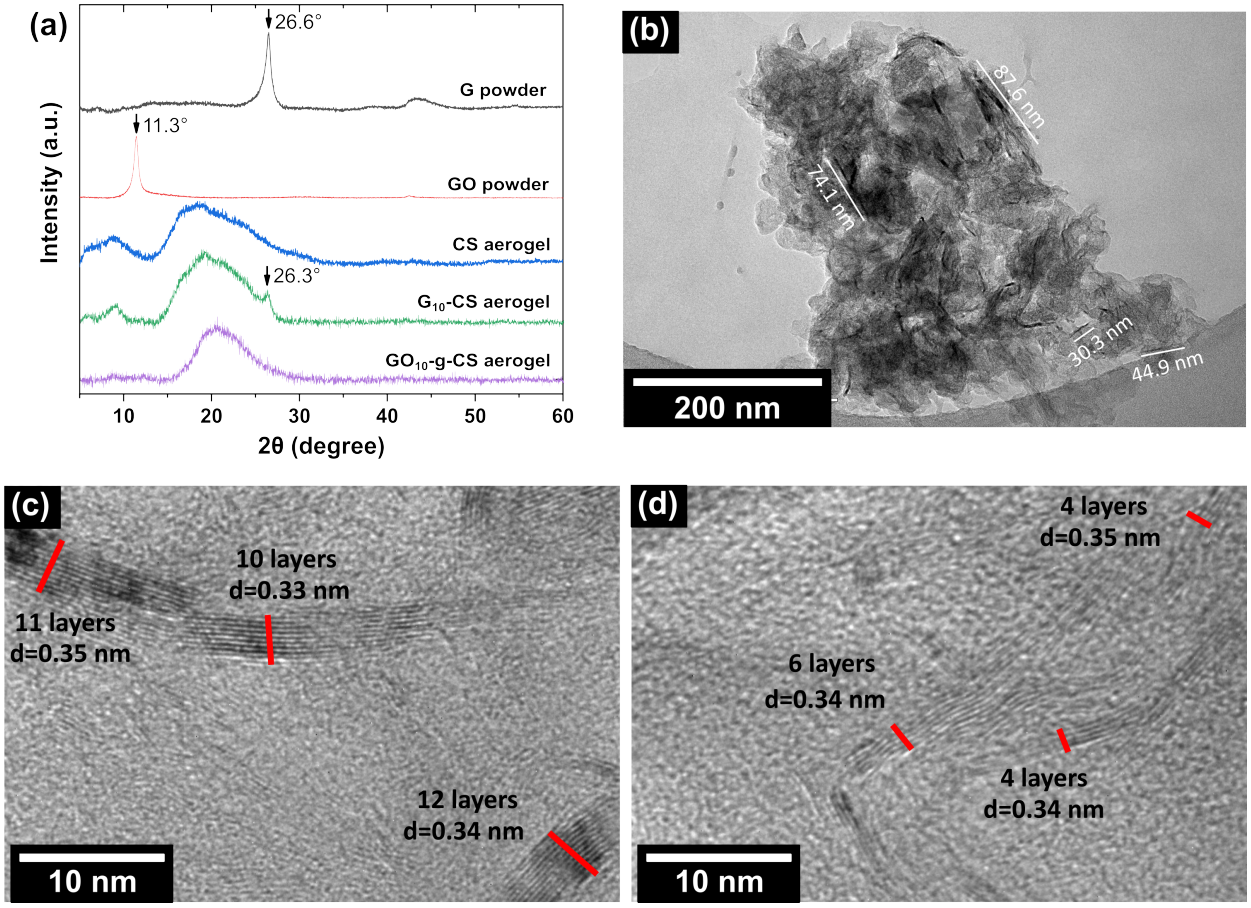

Figure 2: (a) XRD patterns of graphene powder, graphene oxide powder, pure chitosan aerogel, G_{10}-CS aerogel and GO_{10}-g-CS aerogel, (b) low-resolution TEM image, (c) first example of a high-resolution TEM image of G_{10}-CS aerogel, (d) second example of a high-resolution TEM image of G_{10}-CS aerogel.

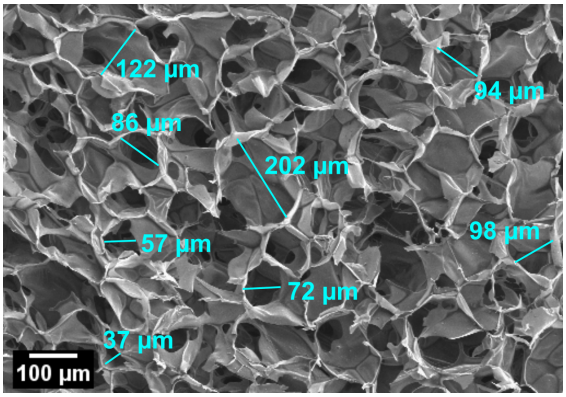

Figure 3: SEM micrograph of G_{10}-CS aerogel.

Cylindrical samples were subjected to a vertical compression test as shown in Fig. 4a. The compressive modulus was calculated as the ratio between stress and strain in the elastic domain, and the resulting value was then averaged from the compression tests conducted on 3 samples. Figure 4b

presents the compressive modulus of graphene-chitosan and chitosan grafted graphene oxide aerogels with varying filler contents, *i.e.* graphene and graphene oxide contents. It is easily seen that the compressive modulus increases as the filler content rises. Specifically, the compressive modulus of the graphene-chitosan aerogel is 0.38 MPa at 10% by weight of graphene, which is approximately 2.8 times higher than the compressive modulus of 0.14 MPa of the pure chitosan aerogel. Meanwhile, a compressive modulus of 0.61 MPa is recorded for the graphene oxide-grafted chitosan aerogel at 10% by weight of graphene oxide, indicating it is around 4.5 times higher than the pure chitosan aerogel. This enhancement can be attributed to the excellent intrinsic stiffness of both graphene and graphene oxide [32, 33], which increases the stiffness of the framework, resulting in improved overall mechanical properties of the aerogel. Furthermore, it can be observed that chitosan grafted graphene oxide aerogels consistently exhibit higher compressive modulus than graphene-chitosan aerogels with the same filler content. This result can be explained by the fact that graphene oxide, due to its abundant functional groups on the surface, can easily be dispersed in the chitosan matrix, forming an exfoliated structure. Simultaneously, graphene oxide also forms covalent bonds through EDC/NHS-mediated reactions with the amino groups in chitosan chains, significantly enhancing the mechanical properties of the aerogels.

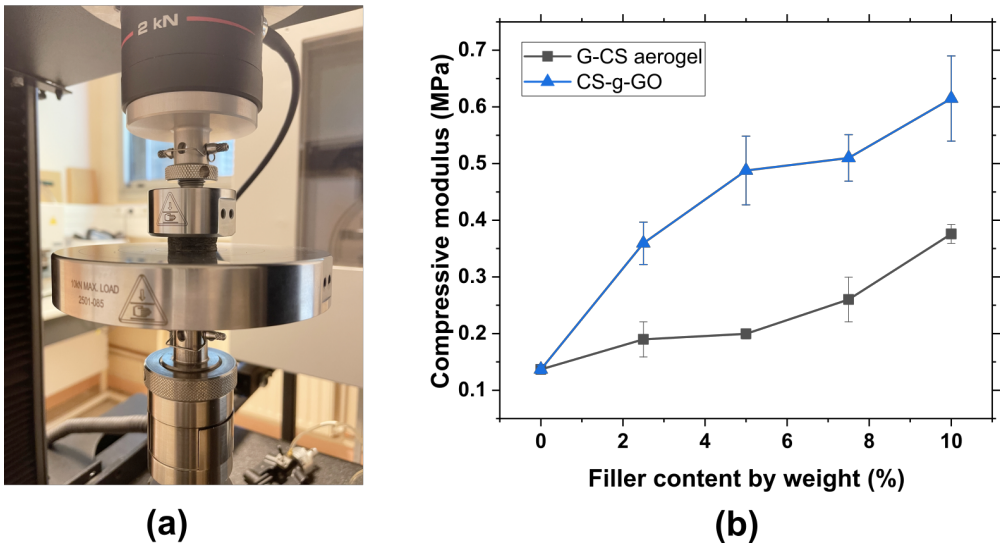

Figure 4: (a) Photographs of the compression test on cylindrical aerogels and (b) compressive modulus as function of filler contents.

3. Multiscale geometrical configuration and materials properties

Based on the experimental results presented in the previous section, the multiscale structure of aerogels was divided into three separate scales. The first scale (scale qualified of nanoscale) was related to the aggregation of graphene sheets (named graphene blocks) or the intercalated structure of graphene oxide (named graphene oxide blocks), the second one corresponded to the microscale where the graphene blocks or graphene oxide blocks dispersed in the chitosan matrix form the solid phase of the aerogel and finally the macroscale was made of gas phase and solid phase as shown in Fig. 5. In this section, the geometrical configurations at different scales are presented and discussed as well as the material properties of the constituents.

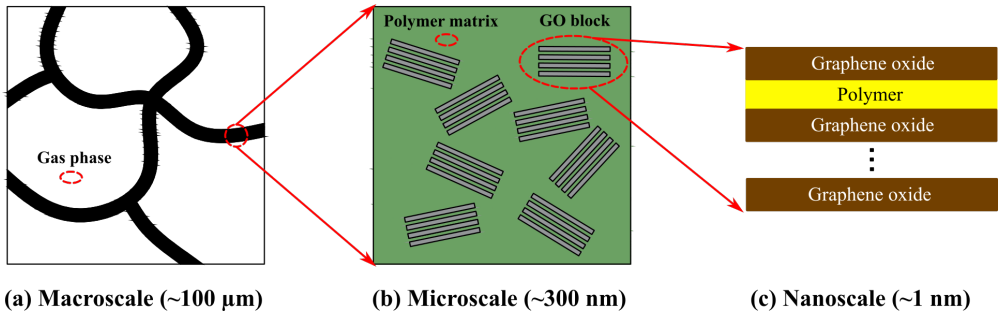

Figure 5: Schematic illustration of the multiscale structure of graphene-chitosan composite aerogels including (a) macroscale depicting solid and gas phases, (b) microscale depicting the distribution of graphene blocks in chitosan matrix and (c) nanoscale describing the graphene sheets in graphene block.

3.1. Construction of multiscale geometrical configuration

3.1.1. Geometrical configuration at the nanoscale

As demonstrated by XRD results and TEM images, the graphene block consists of graphene sheets arranged parallel to each other with a distance of 0.335 nm caused by van der Waals interactions. The number of graphene layers in the blocks was found to vary from 4 to 12 layers. The structure of the graphene block resembles that of crystalline graphite, with different thermal conductivity between the parallel and perpendicular directions to the graphene sheets. Therefore, the geometrical configuration of the graphene block is a homogeneous multilayered assembly with equivalent anisotropic thermal conductivity (see Fig. 6a).

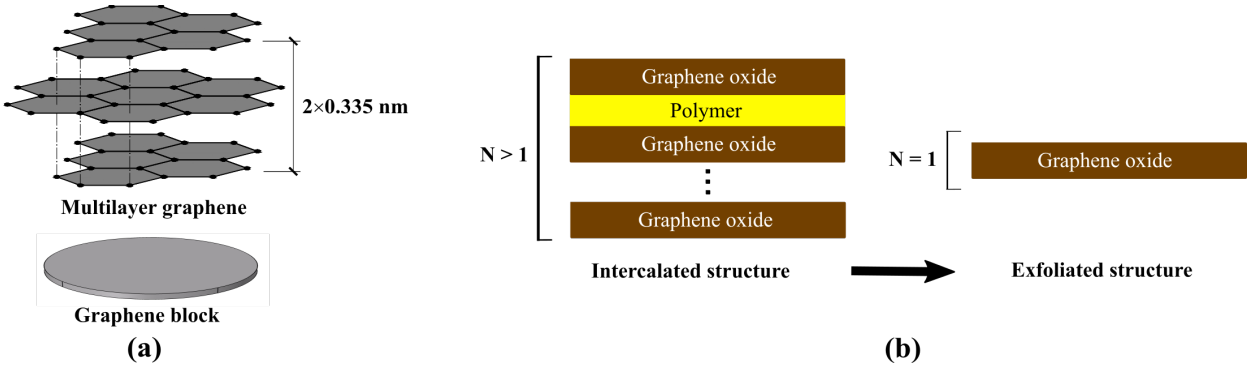

Figure 6: Description of three geometrical configurations at the nanoscale including (a) the aggregate structure of graphene corresponding to graphene block and (b) the intercalated and exfoliated structure of graphene oxide corresponding to graphene oxide block and monolayer graphene oxide, respectively.

For graphene oxide, the intercalated and exfoliated structures are considered as discussed in section 2. The XRD results of graphene oxide powder show that the distance between the sheets is equal to 0.78 nm, which is approximately the thickness of graphene oxide monolayer experimentally measured in previous works [34, 35]. Therefore, the thickness of the graphene oxide sheet is taken as 1 nm. The number of graphene oxide layers per block, denoted by N is greater than 1 for intercalated structure and equal to 1 for exfoliated structure (see Fig. 6b). In the intercalated structure, since the distance between the two graphene oxide layers is in the range of $1.5 - 5.3$ nm [24], the thickness of the polymer (chitosan) interlayer between the graphene oxide layers is taken to be 2 nm.

3.1.2. Geometrical configuration at the microscale

The shape of graphene and graphene oxide is considered to be that of a disc as in previous works [36, 37]. Therefore, each graphene block, graphene oxide monolayer and graphene oxide blocks are also included in the geometrical configuration as disc-shaped inclusions.

With this shape, the diameter and thickness of these inclusions need to be determined. The results from the TEM image in subsection 2.4 show that the graphene blocks have a length of $30.3 - 87.6$ nm and a thickness of $1.36 - 4.04$ nm. Therefore, the aspect ratio of the graphene blocks, defined by the ratio between diameter and thickness, can be estimated in the range of $8 - 65$, which is consistent with the results in previous works [38, 39]. It can be noted that graphene sheets can be disrupted by ultrasonic treatment during graphene dispersion [39], and that the aggregation of graphene layers results in a rather low aspect ratio.

In this work, the typical value of the number of graphene layers and the aspect ratio of the block are taken as 5 and 40, respectively. In addition, it can be seen that the graphene blocks are randomly arranged in the chitosan matrix, they are therefore modeled as discs with arbitrary orientation and position in the polymer matrix.

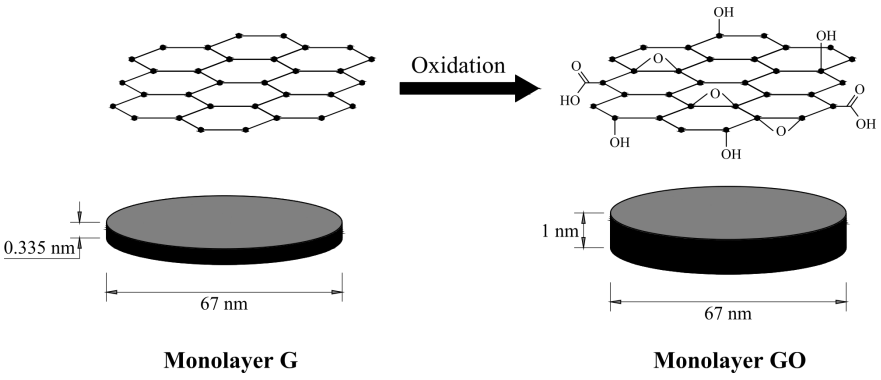

Figure 7: Illustration of the oxidation of graphene to graphene oxide with the lateral dimension unchanged at the nanoscale.

For graphene oxide, the monolayer has an aspect ratio that varies from 10 [40] to more than 1000 [35], depending on the graphene oxide preparation method or the graphene oxide dispersion method in the polymer matrix.

In order to compare the influence of graphene oxide *versus* graphene on the thermal conductivity of aerogels, we assume that the graphene blocks after oxidation form graphene oxide monolayer with constant lateral dimensions. For example, within a typical graphene block having an aspect ratio of 40 and five graphene layers, the monolayered graphene sheets are evaluated to be of equal size with thicknesses and diameters of 0.335 nm and 67 nm, respectively. Therefore, the diameter of the monolayer graphene oxide sheet is also taken to be equal to 67 nm. With a thickness of 1 nm, the aspect ratio of monolayer graphene oxide is equal to 67 (see Fig. 7). For the intercalated structure of graphene oxide, the number of graphene oxide layers per block is investigated at 3 and 5. Additionally, similarly to graphene, the monolayer graphene oxides or graphene oxide blocks are arranged with an arbitrary orientation in the polymer matrix.

Collectively, the representative volume element (RVE) at the microscale consists of disc-shaped inclusions randomly distributed in the polymer matrix with three types of inclusions: graphene block, graphene oxide monolayer and graphene oxide blocks with 3 or 5 layers per block (see

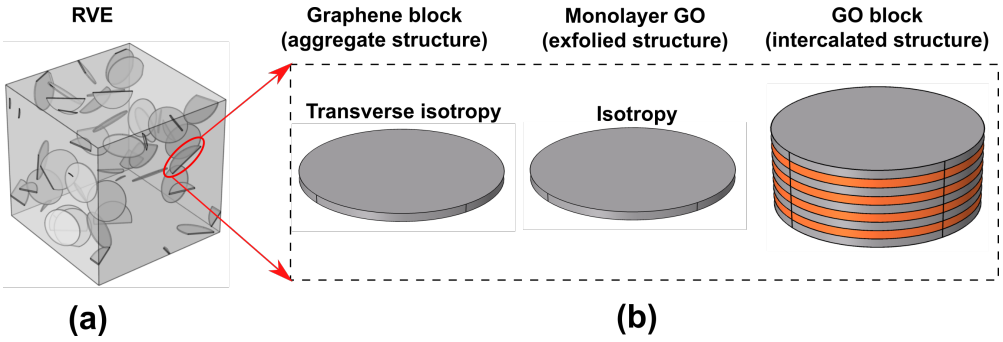

Figure 8: Description of (a) representative volume element at the microscale for 1% concentration by volume of randomly oriented inclusions and (b) three types of inclusions: graphene block, monolayer graphene oxide and graphene oxide block.

Fig. 8).

3.1.3. Geometrical configuration at the macroscale

The geometrical configuration at the macroscale is a periodic structure formed by a single type of repetitive unit cells. The characteristics that must be considered when building this unit cell include pore shape, pore size, and porosity in such a way that the unit cell must represent the material properties of the entire material. According to the application of aerogels, two main morphologies of aerogels are taken into consideration in the literature, leading to an anisotropic or isotropic behavior of the structure that is obtained by using different freezing techniques. Two controlled freezing techniques are utilized to create the anisotropic structure: unidirectional freezing produces a structure with tubular pores parallel to the freezing direction [5], while bidirectional freezing affords a structure with parallel layered lamellars [41]. For the isotropic structure, the aerogels were frozen by ensuring freezing in all directions at the same freezing rate. By using this freezing method, the aerogels obtained in our research featured a cellular structure with an interconnected pore network whose average pore diameter was equal to 76 μm. This conclusion agreed with other studies [6, 5] that used the same freezing procedure and observed a pore size ranging from a few tens to several hundreds of micrometers.

Next, the Cartesian reference system is used in which the orthonormal basis is denoted by $(\mathbf{e}_1, \mathbf{e}_2, \mathbf{e}_3)$ and the position vector at macroscopic scale by $\mathbf{x} = (x_1, x_2, x_3)$.

In this study, the unit cell representing the macrostructure of the material is a hollow sphere with a diameter of 76 μm as shown in Fig. 9c. Six holes with a diameter of 12 μm were made on the wall of the hollow sphere to create the interconnected pore network among the unit cells.

In addition to the aforementioned factors, the wall thickness of the hollow sphere must be determined to fully describe the unit cell. This thickness is determined by introducing the porosity of the unit cell which is the volume fraction of gas phase in the unit cell. Due to the periodicity, the relationship between aerogel porosity and aerogel density has been used to calculate the porosity of aerogel. This relationship is expressed by the following expression:

$$\phi_a = 1 - \frac{\rho_a}{\rho_s}, \tag{1}$$

where ϕ_a and ρ_a are the porosity and the apparent mass density of aerogel, respectively. The quantity ρ_s is the mass density of the solid phase related to the mass density of the graphene ρ_G

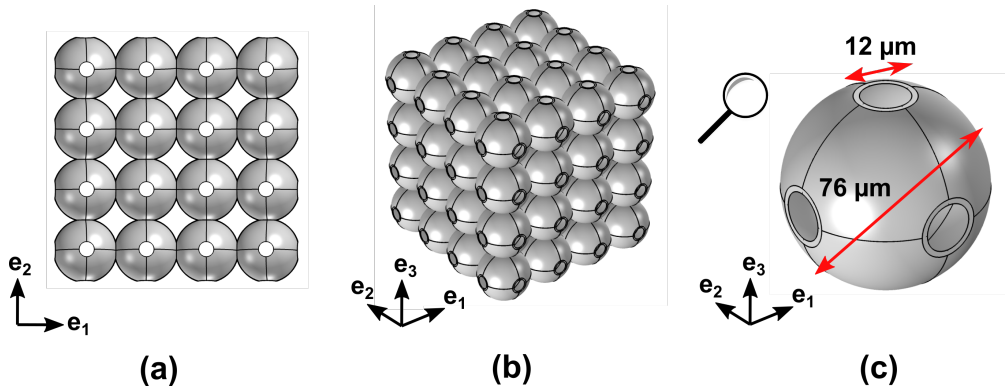

Figure 9: (a) The three-dimensional view of the overall geometrical configuration as an array consisting of periodic unit cells along the $\mathbf{e}_1$, $\mathbf{e}_2$ and $\mathbf{e}_3$ directions; (b) the representative unit cell and (c) the vertical view of the geometrical configuration at the macroscale.

and chitosan ρ_{CS} components by the following expression:

$$\rho_s = f_v \rho_G + (1 - f_v)\rho_{CS}, \tag{2}$$

where f_v is the graphene volume fraction, defined as the ratio of the volume of graphene to the volume of the RVE. In the experiment, graphene was added to the polymer as a percentage by mass of polymer f_w. Therefore, for instance, the relation between f_v and f_w in aerogel is given by the relation:

$$f_v = \frac{\rho_{CS} f_w}{\rho_{CS} f_w + \rho_G}. \tag{3}$$

Table 1: Apparent mass density and calculated porosity of aerogels.

Graphene weight fraction f_w (%)	Graphene volume fraction f_v (%)	Apparent mass density ρ_a (g.cm^{-3})	Porosity ϕ_a (%)
0	0	0.0256 ± 0.0012	98.25 ± 0.08
2.5	1.59	0.0261 ± 0.0010	98.23 ± 0.06
5	3.13	0.0262 ± 0.0002	98.24 ± 0.01
7.5	4.62	0.0277 ± 0.0006	98.15 ± 0.04
10	6.06	0.0290 ± 0.0014	98.08 ± 0.09

For pure chitosan aerogel, the value of ρ_{CS} is taken to be equal to 1.463 g.cm^{-3} [42]. The mass density of graphene is taken to be equal to the mass density of crystalline graphite which is equal to $\rho_G = 2.267$ g.cm^{-3} [43]. Given the measured apparent mass densities of the aerogels, their overall porosity is shown in Tab. 1. It can be seen that the porosity of the aerogel does not change significantly as the graphene weight fraction f_w varies; especially when the graphene weight ratio is below 5% (corresponding to the graphene volume fraction below 3%), the porosity barely varies by 98.231 to 98.250%. This results is consistent with previous works [5, 44]. For the graphene oxide-grafted aerogel, its porosity was calculated in a similar way, where the mass density of graphene oxide is taken to be 2 g.cm^{-3} (see [45]). Similar results have also been obtained for this type of aerogel.

Therefore, in the parametric study, the value of aerogel porosity is taken with an average value of 98.24% and the values of graphene and graphene oxide volume fraction f_v are taken in the range of $0 - 3\%$.

3.2. Material properties of the constituents

Graphene is known for its high in-plane thermal conductivity. At room temperature, the in-plane thermal conductivity of graphene is in the range of $2000 - 4000$ W/(m·K) [46]. However, when graphene sheets are closely packed due to weak van der Waals interactions forming blocks, the thermal conductivity of these multilayer blocks in the out-of-plane direction (the direction perpendicular to the sheets) is much weaker than in the in-plane direction. Indeed, the out-of-plane thermal conductivity of pyrolytic graphite at room temperature is only about 6 W/(m·K) [46]. In this work, graphene blocks are introduced into the model with in-plane and out-of-plane thermal conductivity values of 2500 W/(m·K) and 6 W/(m·K), respectively.

It has been indicated that graphene oxide has significantly lower thermal conductivity compared to graphene due to the phonon-defect scattering at the surface oxidized groups, which reduces the overall phonon mean free path of graphene oxide [47, 48]. The thermal conductivity of graphene oxide is taken as 18 W/(m·K), as measured experimentally in the work of Mahanta and Abramson [48]. Therefore, the graphene oxide monolayer is considered as an isotropic material with thermal conductivity of 18 W/(m·K) [48]. For graphene oxide blocks, the effective thermal conductivity is calculated using Milton's method, which will be detailed in the following section.

Most of polymers are thermally insulating exhibiting thermal conductivity ranging from 0.1 to 0.5 W/(m·K) [49]. In this study, the polymer matrix is considered as isotropic and homogeneous with a thermal conductivity of 0.2 W/(m·K).

4. Homogenization method

4.1. Determination of material properties of graphene oxide block at the nanoscale

In this section, we calculate the effective thermal conductivity of the graphene oxide blocks for the intercalated structure which will be used at the microscale to describe homogeneous inclusions embedded in the polymer matrix. With a laminate structure of graphene oxide blocks consisting of alternating graphene oxide and polymer layers, the Milton's method [50] is relevant to determine the effective thermal conductivity of a graphene oxide block. By using the Milton's method, the effective thermal conductivity tensor of laminate materials with arbitrary layer orientations can be obtained. This is in perfect agreement with our model where stratified inclusions are oriented randomly in a matrix.

The following paragraph introduces the method principle for calculating the effective thermal conductivity tensor of a two-phase laminate material. We consider a laminate domain Ω consisting of two phases, assuming that there is no volumetric heat source, the steady state heat conduction equations of each phase are given as follows:

$$\mathbf{q}(\mathbf{x}) = \mathbf{K}(\mathbf{x})\,\mathbf{G}(\mathbf{x}), \tag{4}$$

$$\mathbf{G} = -\mathrm{grad}\ T, \tag{5}$$

$$\mathrm{div}\,\mathbf{q} = 0, \tag{6}$$

where the thermal heat flux is denoted by $\mathbf{q}$, $\mathbf{G}$ denotes the temperature gradient, T is the temperature, $\mathbf{K}$ is the second-order thermal conductivity tensor, div is the divergence operator and grad

is the gradient operator. These equations are derived from the physical laws of conduction of heat by using Fourier's law and conservation of energy.

The main idea of this method involves seeking solutions to the partial differential equations by assuming that specific components of the fields are constant or, equivalently, that specific projections of the fields are uniform. It is assumed that $\mathbf{q}, \mathbf{G}$ and $\mathbf{K}$ vary only in the direction of the layers, characterized by the unit vector $\mathbf{n}$:

$$\mathbf{q} = \mathbf{q}(y), \quad \mathbf{K} = \mathbf{K}(y), \quad \mathbf{G} = \mathbf{G}(y) \qquad \text{where } y = \mathbf{x} \cdot \mathbf{n}. \tag{7}$$

It is easily obtained that there are no variations in the component of $\mathbf{q}$ and $\mathbf{G}$ that are parallel and perpendicular to $\mathbf{n}$, respectively, that is:

$$\mathbf{n} \cdot \mathbf{q} = \mathbf{n} \cdot \langle \mathbf{q} \rangle_\Omega, \qquad \mathbf{G} = \langle \mathbf{G} \rangle_\Omega + \frac{d\tilde{T}(y)}{dy}\,\mathbf{n}, \tag{8}$$

where $d\tilde{T}(y)/dy$ is the fluctuating part of the temperature gradient in the direction parallel to $\mathbf{n}$ ensuring the condition $\tilde{T}(y)$ is periodic over Ω and the symbol $\langle \star \rangle_\Omega$ denotes the volume average of $\star$ over domain Ω.

Introducing the two matrices $\mathbf{\Gamma}_1(\mathbf{n})$ and $\mathbf{\Gamma}_2(\mathbf{n})$ which are the projections on the out of plane and the plane of normal $\mathbf{n}$, Eq. (8) implies that:

$$\mathbf{\Gamma}_1(\mathbf{n})\mathbf{q} = \mathbf{\Gamma}_1(\mathbf{n})\langle \mathbf{q} \rangle_\Omega, \qquad \mathbf{\Gamma}_2(\mathbf{n})\mathbf{G} = \mathbf{\Gamma}_2(\mathbf{n})\langle \mathbf{G} \rangle_\Omega, \tag{9}$$

where $\mathbf{\Gamma}_1(\mathbf{n})$ and $\mathbf{\Gamma}_2(\mathbf{n})$ are represented as functions of the vector $\mathbf{n}$ as follows:

$$\mathbf{\Gamma}_1(\mathbf{n}) = \mathbf{n} \otimes \mathbf{n}, \qquad \mathbf{\Gamma}_2(\mathbf{n}) = \mathbf{I} - \mathbf{n} \otimes \mathbf{n}, \tag{10}$$

with $\mathbf{I}$ is the second-order identity tensor and the symobol $\otimes$ denotes the tensor product (also called dyadic product of two vectors).

It is noteworthy that $\mathbf{\Gamma}_1(\mathbf{n})$ and $\mathbf{\Gamma}_2(\mathbf{n})$ are projections onto mutually orthogonal subspaces satisfying the expected properties:

$$\mathbf{\Gamma}_i(\mathbf{n})\,\mathbf{\Gamma}_j(\mathbf{n}) = \delta_{ij}\mathbf{\Gamma}_i(\mathbf{n}), \text{for i,j} = 1,2 \qquad \text{and} \qquad \mathbf{\Gamma}_1(\mathbf{n}) + \mathbf{\Gamma}_2(\mathbf{n}) = \mathbf{I}, \tag{11}$$

where δ_{ij} is Kronecker's symbol.

To determine the effective conductivity tensor, the polarization field $\mathbf{p}$ is introduced:

$$\mathbf{p}(\mathbf{x}) = (\mathbf{K}(\mathbf{x}) - c_0\,\mathbf{I})\mathbf{G}(\mathbf{x}) = \mathbf{q}(\mathbf{x}) - c_0\mathbf{G}(\mathbf{x}), \tag{12}$$

where c_0 is an arbitrary constant that can be freely chosen. From Eq. (12), the temperature gradient $\mathbf{G}(\mathbf{x})$ and its average $\langle \mathbf{G}(\mathbf{x}) \rangle_\Omega$ can be expressed in terms of the polarization field $\mathbf{p}$ and its average $\langle \mathbf{p}(\mathbf{x}) \rangle_\Omega$:

$$c_0\,\mathbf{G}(\mathbf{x}) = -\mathbf{M}(\mathbf{x})\,\mathbf{p}(\mathbf{x}), \quad c_0\,\langle \mathbf{G}(\mathbf{x}) \rangle_\Omega = \mathbf{M}^e\,\langle \mathbf{p}(\mathbf{x}) \rangle_\Omega, \tag{13}$$

where the following two second-order tensors have been introduced:

$$\mathbf{M}(\mathbf{x}) = c_0\,(c_0\,\mathbf{I} - \mathbf{K}(\mathbf{x}))^{-1}, \quad \mathbf{M}^e = c_0\,(c_0\,\mathbf{I} - \mathbf{K}^e)^{-1}, \tag{14}$$

where the superscript e designates the average of the field.

By using Eq. (12), one shows that the polarization field average can be formulated as follows:

$$\langle \mathbf{p}(\mathbf{x}) \rangle_\Omega = [\mathbf{M}^e - \boldsymbol{\Gamma}_1(\mathbf{n})]^{-1}\, \mathbf{v} = \langle [\mathbf{M}(\mathbf{x}) - \boldsymbol{\Gamma}_1(\mathbf{n})]^{-1} \rangle_\Omega\, \mathbf{v}, \tag{15}$$

for all uniform fields $\mathbf{v}$.

Since Eq. (15) holds for all fields $\mathbf{v}$, this relation implies the general formula given by:

$$[\mathbf{M}^e - \boldsymbol{\Gamma}_1(\mathbf{n})]^{-1} = \langle [\mathbf{M}(\mathbf{x}) - \boldsymbol{\Gamma}_1(\mathbf{n})]^{-1} \rangle_\Omega. \tag{16}$$

With these relations, the calculus of the effective thermal conductivity tensor $\mathbf{K}^e$ is carried out as follows:

1. evaluation of: $\mathbf{L} = \langle [\mathbf{M}(\mathbf{x}) - \boldsymbol{\Gamma}_1(\mathbf{n})]^{-1} \rangle_\Omega$,
2. from Eq. (16), evaluation of: $\mathbf{M}^e = \mathbf{L}^{-1} + \boldsymbol{\Gamma}_1(\mathbf{n})$,
3. from Eq. (14), evaluation of: $\mathbf{K}^e = c_0\, (\mathbf{I} - (\mathbf{M}^e)^{-1})$.

4.2. Asymptotic homogenization procedure for micro- and macroscales homogenization

The asymptotic method is a powerful tool for solving periodic domain problems. The details of the homogenization method can be easily found in the literature, for example in the books of Auriault *et al.* [17] and Mei *et al.* [51]. In this subsection, the principle and the main results of this method are presented.

We consider a two-phase composite material with a periodic domain. The microscopic domain of a unit cell is denoted by Y (include in the three-dimensional space), corresponding to the period l_c which is the microscopic characteristic length. In contrast, the characteristic length at the macroscale, as denoted by L_c, is noticeably separated from the microscopic length, that is, $l_c/L_c = \epsilon \ll 1$. Domain Y is composed of phase a and phase b, occupying the domains Y^a and Y^b, respectively, and their interface Γ.

$$Y = Y^a \cup Y^b, \quad Y^a \cap Y^b = \emptyset, \quad \partial Y^a \cup \partial Y^b = \Gamma. \tag{17}$$

4.2.1. Microscopic scale governing equations

In this subsection, in each phase $\alpha = a, b$, the temperature is denoted by T^α and the second-order thermal conductivity tensor is denoted by $\mathbf{K}^\alpha$.

Assuming that there is no volumetric heat source, the steady-state heat conduction problem is described by the following equations:

$$\operatorname{div}(\mathbf{K}^\alpha \operatorname{grad} T^\alpha) = 0 \quad \text{in } Y^\alpha, \text{ for } \alpha = a, b. \tag{18}$$

Assuming perfect thermal contact between phase a and phase b, the continuity conditions in the heat transfer problem are as follows:

$$T^a = T^b, \quad \text{on } \Gamma, \tag{19}$$

$$(\mathbf{K}^a \operatorname{grad} T^a - \mathbf{K}^b \operatorname{grad} T^b) \cdot \mathbf{n} = 0, \quad \text{on } \Gamma, \tag{20}$$

where $\mathbf{n}$ is the outward-pointing unit vector locally normal to the boundary Γ.

4.2.2. Asymptotic expansions

As we defined above, l_c represents the unit length of the periodicity and L_c represents the length at the macroscale so that the condition $l_c/L_c = \epsilon \ll 1$ is satisfied. We introduce now the fast and slow coordinates $\mathbf{x} = (x_1, x_2, x_3)$ and $\mathbf{y} = (y_1, y_2, y_3)$ for coordinates at macro- and microscales, respectively, with the relationship $y_i = x_i/\epsilon$.

The asymptotic expansion of temperature is expanded as a power series of ϵ as follows:

$$T^{\alpha} = T^{\alpha(0)}(\mathbf{x}, \mathbf{y}) + \epsilon T^{\alpha(1)}(\mathbf{x}, \mathbf{y}) + \epsilon^2 T^{\alpha(2)}(\mathbf{x}, \mathbf{y}) + ... \tag{21}$$

where $T^{\alpha(0)}, T^{\alpha(1)}, T^{\alpha(2)}$,... are Y-periodic in the variable $\mathbf{y}$. Terms of the order of ϵ^n are represented by the upper index (n), where macroscale variables are expressed in the order of ϵ^0.

4.2.3. Cell problem and effective properties

By substituting Eq. (21) into Eqs. (18) at order ϵ^{-2}, Eq. (19) at order ϵ^0 and Eq. (20) at order ϵ^{-1}, we get $T^{\alpha(0)}$ is a constant with respect to $\mathbf{y}$, that is, $T^{a(0)}(\mathbf{x}, \mathbf{y}) = T^{b(0)}(\mathbf{x}, \mathbf{y}) = T^{(0)}(\mathbf{x})$.

Grouping ϵ^{-1} terms of Eq. (18), ϵ terms of (19) and ϵ^0 terms of (20), in virtue of the linearity of the problem, the Y-periodic characteristic vector-valued function $\mathbf{w}^{\alpha}(\mathbf{y})$ (whose the components are given by $w_l^{\alpha}(\mathbf{y})$) is introduced so that:

$$T^{\alpha(1)}(\mathbf{x}, \mathbf{y}) = w_l^{\alpha}(\mathbf{y}) \frac{\partial T^{(0)}(\mathbf{x})}{\partial x_l} + \bar{T}^{\alpha(1)}(\mathbf{x}), \tag{22}$$

where $\bar{T}^{\alpha(1)}(\mathbf{x})$ is a constant field with respect to $\mathbf{y}$. This relation leads to the cell problem defined by:

$$\frac{\partial}{\partial y_i}\left[K_{ij}^{\alpha}\left(\frac{\partial w_l^{\alpha}}{\partial y_j} + \delta_{jl}\right)\right] = 0, \quad \text{in } Y^{\alpha},\ \alpha = a, b \tag{23}$$

$$w_i^a = w_i^b, \text{ on } \Gamma \tag{24}$$

$$K_{ij}^{a}\left(\frac{\partial w_l^{a}}{\partial y_j} + \delta_{jl}\right) n_i = K_{ij}^{b}\left(\frac{\partial w_l^{b}}{\partial y_j} + \delta_{jl}\right) n_i, \quad \text{on } \Gamma \tag{25}$$

$$\langle \mathbf{w} \rangle_Y = 0, \tag{26}$$

where δ_{ij} is Kronecker symbol and $\langle \star \rangle_Y$ denotes the volume average of $\star$ over domain Y:

$$\langle \star \rangle_Y = \frac{1}{Y}\left\{\int_{Y^a} (\star) dV + \int_{Y^b} (\star) dV\right\}. \tag{27}$$

The condition given in Eq. (26) is a normalization condition to render the solution for $\mathbf{w}^{\alpha}$ unique.

At order ϵ^0 of Eq. (18), order ϵ^2 of Eq. (19) and order ϵ of Eq. (20), the macroscopic equation can be written as:

$$\text{div}\left(\mathbf{K}^e \text{grad}\, T^{(0)}(\mathbf{x})\right) = 0 \quad \text{in } Y, \tag{28}$$

where the components of the effective thermal conductivity tensor are given by

$$K_{ij}^{e} = \left\langle K_{il}^{\alpha}\left(\frac{\partial w_j^{\alpha}}{\partial y_l} + \delta_{jl}\right)\right\rangle_Y. \tag{29}$$

The effective thermal conductivity tensor can be determined from Eq. (29) from the solution of the cell problem defined by Eqs. (23)-(26).

5. Results and discussion

5.1. Numerical implementation

To perform numerical studies on the effective thermal conductivity of materials using a multi-scale approach, problems were solved successively from the small to the larger scale by introducing the result of the smaller scale into the subsequent larger scale. In addition, the interface between the inclusions and the polymer matrix was considered perfectly bonded in this modelling.

At the nanoscale, the thermal conductivity of the graphene blocks was assumed to be the same as that of graphite with experimentally measured values [46], implying that the graphene block exhibited transverse isotropic characteristics. Besides, the effective thermal conductivity tensor of graphene oxide block was easily obtained by the semi-explicit formulas. Specifically, the effective thermal conductivity of the graphene oxide blocks exhibited transverse isotropy, similarly to the graphene blocks. The thermal conductivity of the graphene oxide blocks with 3 layers in the parallel and perpendicular directions to the sheets were equal to 7.8 W/(m·K) and 0.3 W/(m·K), respectively. Meanwhile, these values were equal to 7.0 W/(m·K) and 0.3 W/(m·K) for the graphene oxide block with 5 layers, respectively.

For the calculation of the effective thermal conductivity tensor at the micro- and macroscales through Eq. (29) in the asymptotic approach, the function $\mathbf{w}^{\alpha}$ must first be determined in the cell problem given by Eqs. (23)-(26). To do so, the finite element method was used and simulations were carried out using the Comsol Multiphysics software [52]. The following paragraphs summarize the problem solving process at the micro- and macroscales by using the finite element (FE) method.

At the microscale, the algorithm used to implement the 3D FE model results from the combination of seamless integration of Comsol Multiphysics with Matlab. The algorithm written in Matlab allows for the generation of the representative volume element (RVE) with randomly distributed inclusions as well as the introduction of effective thermal conductivity values of inclusions and polymer matrix into the model. These two processes are described in detail below.

Generation of random disc-shaped inclusions

The geometrical construction of disc-shaped inclusions randomly placed in a given volume domain is carried out by using a method proposed elsewhere [53]. This method, which has previously been introduced [54] for discs-shaped in 2D and spheres-shaped in 3D, uses an algorithm based on molecular dynamics. In this algorithm, all particle (inclusions) are randomly created with a null volume within a cube of specified dimensions. A random velocity vector is prescribed at each particle. The particles are then set in motion and each volume gradually increases from zero. Two types of incidents are checked at each iteration: binary collisions and collisions between particles and the cell faces. When a binary collision occurs, with respect to the kinetic energy conservation principle, the velocities of the two concerned particles are updated. Nevertheless, if a particle leaves the volume domain through a face, it must appear from the opposite side to carry out the periodicity conditions. The simulation stops when the imposed volume fraction is reached. This algorithm is more efficient than the random sequential adsorption algorithm [55, 56], in particular, it can generate very dense packings in a low computation time.

The principal steps of the algorithm are summarized hereafter.

(i) N ellipsoids are randomly created within a cube domain of side L. The volume of each ellipsoid is initially null. At each ellipsoid is attributed a random velocity, an angular velocity and a random orientation.

(ii) The growth rates of the semi-principal axes a_0, b_0, c_0 of ellipsoid are chosen in such a way that $b_0 = a_0/r_1$ and $c_0 = a_0/r_2$, where r_1 and r_2 denote respectively the two aspect ratios that serve as inputs in the algorithm.

(iii) The elliptical particles are then put in translational and rotational motion and their volumes gradually increase. At each step, two types of collisions are checked and computed: binary collision between two ellipsoids and collision between a particle and a cube domain face. If the first type of collision occurs, the velocity and angular velocity of the involved particles are updated. However, if an ellipsoid intersects a cube domain face, its periodic image is created on the opposite side.

(iv) The algorithm stops when the volume fraction ϕ is reached.

(v) The ellipsoid is then completely replaced by discs by keeping their position, orientation, aspect ratio and volume. The model is then returned to the actual size with the reference of the thickness of the graphene sheet.

(vi) Finally, a visual check is performed to check the presence of overlaps among the particles or between the particles and the RVE surface.

Input properties of the inclusions

(i) It should be noted that this process is only necessary when the inclusions are not isotropic, that is, for graphene block and graphene oxide blocks.

(ii) A loop is created, where the effective thermal conductivity tensor of each graphene oxide block is calculated using Milton's equation directly (as described in section 4.1). For the graphene block, its effective thermal conductivity tensor is applied to the model using the rotation of its unit vector towards the corresponding direction in the matrix polymer.

For the finite element method, the domain and the equations were discretized on an unstructured mesh of tetrahedral finite elements with quadratic Lagrange interpolating polynomials. The meshing process was conducted in 2 steps starting by the inclusions then the polymer matrix with the maximum element size of the inclusion of 5 nm, and the maximum element size of the matrix of 1/5 of the RVE size. The MUltifrontal Massively Parallel sparse direct Solver (MUMPS) method with the relative tolerance of 0.001 was used for the final linear system. In addition, periodic boundary conditions were imposed due to the periodicity of the model. An example of a meshed specimen of a RVE at the microscale with inclusions being graphene oxide monolayers is shown in Fig. 10a.

At the macroscale, the surface thickness of the hollow sphere was controlled to construct the unit cell with the desired porosity. Here, the effective thermal conductivity tensor obtained from the results of microscale is introduced into the solid phase. Then, the cell problem solving procedure for calculating the function $\mathbf{w}^{\alpha}$ for the unit cell and followed by the effective thermal conductivity tensor is carried out with the same finite element method as that in the microscale. For meshing, the maximum element size of the solid and gas phases is equal to twice the surface thickness of the hollow sphere and 1/5 of the representative unit cell size, respectively. Figure 10b presents an example of a meshed specimen of representative unit cell at the macroscale with a porosity of 98.24% corresponding to a surface thickness of 1.24 μm.

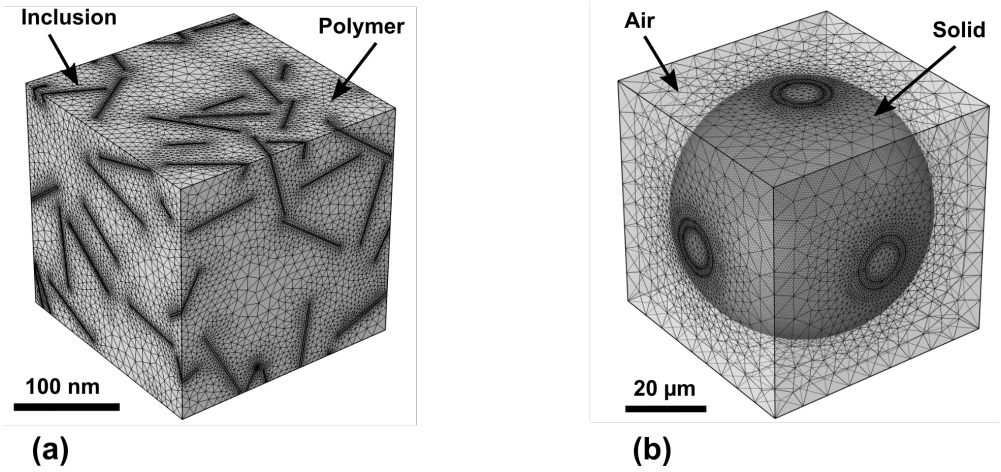

Figure 10: Example of a meshed specimen of (a) a RVE at the microscale with 2% inclusion volume fraction and 40 inclusions and (b) a representative unit cell at the macroscale consisting of solid and gas phases with porosity of 98.24%.

In the following section, for the sake of brevity, the exponent ^{e} referring to the effective properties is dropped. Instead, the exponents $^{(2)}$ and $^{(3)}$ characterize computational quantities at the micro-, and macroscales, respectively.

5.2. Effective thermal conductivity of composite aerogels at the microscale

5.2.1. RVE size sensitivity

At the microscale, we start by testing the influence of RVE size on the estimated effective thermal conductivity. Given the determined shape and volume fraction of inclusions, the size of the RVE is directly related to the number of inclusion considered. Therefore, in small RVEs, the random inclusion distribution can be distorted due to the low number of inclusions, resulting in a variation in the results obtained. Nevertheless, too large RVE size also requires high computational cost. Finding a reasonable size of the RVE to exhibit convergence of the outcome was therefore the target of this subsection. To do that, we consider the case of graphene oxide monolayer with volume fraction $f_v = 1\%$, the RVE size was thus determined by varying the number of inclusions from 10 to 60, with increments of 10. At each defined number of inclusions, we calculate all the components K_{ij} of the effective thermal conductivity tensor $\mathbf{K}^{(2)}$ of 5 RVEs where the microstructural morphology was independently generated. Here, the thermal conductivity of graphene oxide and polymer are spherical tensors characterized by scalar values of 18 W/(m·K) and 0.2 W/(m·K), respectively.

Figure 11a presents the components K_{ij} of the effective thermal conductivity tensor $\mathbf{K}^{(2)}$ in all 5 cases in which 30 inclusions were generated. It is easy to see that the composite at the microscale is almost isotropic, that is $\mathbf{K}^{(2)} = K^{(2)}\,\mathbf{I}$. This complies with the principle of random inclusion distribution in the polymer matrix, partly demonstrating the validity of the proposed model. Moreover, the variations of K_{11}, K_{22} and K_{33} are also observed. By introducing this variation as a function of the number of inclusions, the effect of RVE size on the convergence of the results can be observed.

Figure 11b shows the variation of the effective thermal conductivity normalized by the thermal conductivity of the polymer matrix $\mathbf{K}_m = K_m\,\mathbf{I}$ as a function of the number of inclusions from 10 to 60. The results indicate that the effective thermal conductivity is insensitive to the RVE size

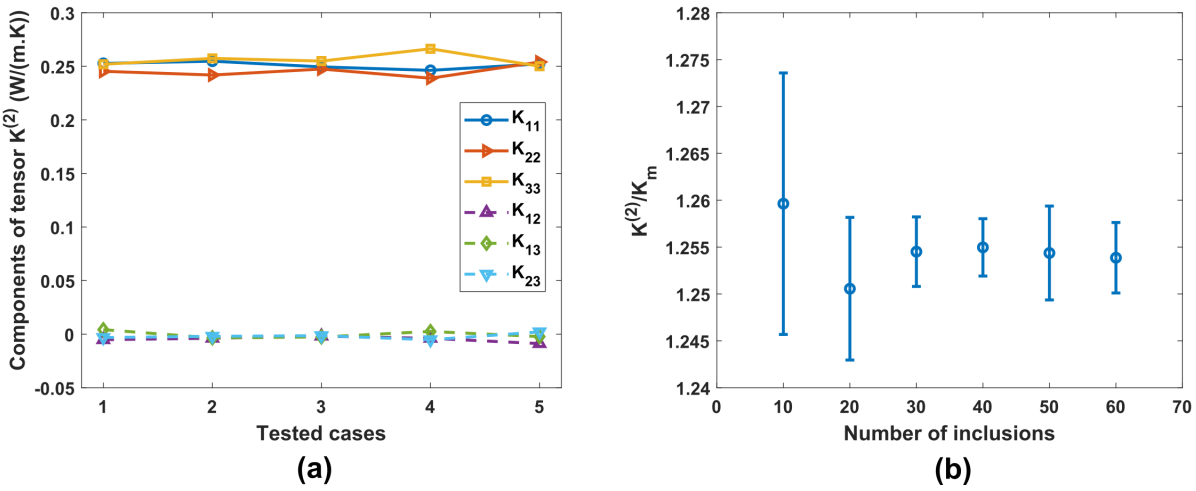

Figure 11: (a) Variation of the components of the effective thermal conductivity tensor for different configurations of graphene oxide monolayer with $f_v = 1\%$ (RVE sizes were built with 30 inclusions) and (b) effect of number of inclusion (RVE size) on the effective thermal conductivity at the microscale.

when more than 30 inclusions were present in the domain. This number of inclusions is consistent with previous reports in the literature [57, 58]. In the subsequent study, the number of inclusions in the RVE will be used from 30 to 50 corresponding to the inclusion volume fraction from 1 to 3%.

5.2.2. Effect of graphene oxide on the thermal conductivity of composite

Although graphene oxide has a low thermal conductivity (18 W/(m·K)) [48], it is still used to enhance the heat transfer capacity of polymer matrix due to its low production cost and good dispersion ability as well as its stability in the polymer matrix [59, 60]. This subsection draws on experimental works on the thermal conductivity of composite materials based on graphene oxide and polymer (epoxy resin) [59, 60] in order to comprehend the effect of structural factors, *i.e.* exfoliated or intercalated structures, on the effective thermal conductivity of composite materials at the microscale and to validate the robustness of the proposed model at this scale. For this purpose, the effective thermal conductivity of composites with exfoliated structure (1 single layer) or intercalated structure (3 or 5 layers per block) at the microscale is depicted as a function of the volume fraction of graphene oxide (as shown in Fig. 12a). It is clearly observed that in all cases the thermal conductivity increases as the volume fraction of graphene oxide increases with a (nearly) linear relationship. Additionally, the exfoliated structure can improve the thermal conductivity of the composite substantially more than the intercalated structure. In particular, the composite with onelayer, 3 layers, and 5 layers of graphene oxide per block at 3% graphene oxide volume fraction improved in the thermal conductivity by 82%, 45%, and 35%, respectively, compared to the pure polymer. This may be explained by the fact that when the number of graphene oxide layers per block increases, the aspect ratio of the block (inclusion) decreases, thus lowering the heat conductivity of the composite [61]. The mechanical properties of graphene-reinforced polymer have also been shown to follow a similar trend [62]. These results demonstrate the effectiveness of using graphene oxide to simultaneously improve the heat transfer capacity and mechanical properties of the polymer matrix. With the aim of producing a material with improved thermal insulation and high mechanical strength, the latter statement raises the question of whether, the addition of

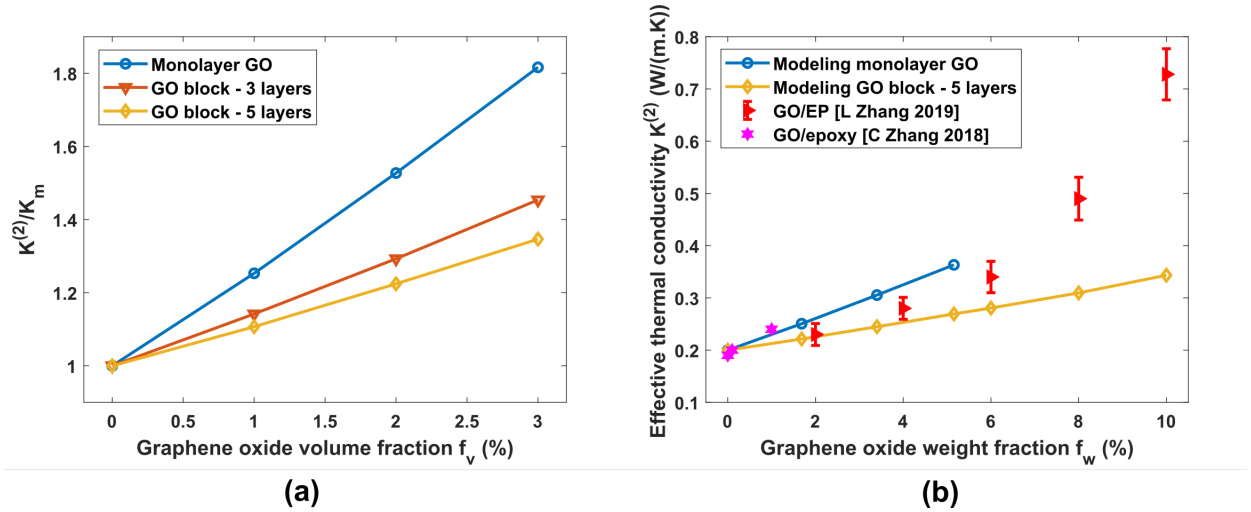

Figure 12: (a) Effect of the inclusion type-related structural parameter on the thermal conductivity of aerogel and (b) numerical predictions of the effective thermal conductivity at the microscale compared to the experimental data of graphene oxide/epoxy composites from [59, 60].

graphene or graphene oxide to enhance the mechanical properties of polymer-based aerogels leads to an increase of its thermal conductivity as well. In other words, how will the amount of graphene or graphene oxide affect the thermal conductivity of this aerogel at the macroscale, where the gas phase occupies most of the material's volume? In the following section, the estimated thermal conductivity at the macroscale will be presented, which will answer this question.

Before proceeding to the next larger scale, we also compared the thermal conductivity of the material at the microscale predicted by our model with that extracted from experimental measurements in literature. To do that, the graphene oxide volume fraction was converted to graphene oxide weight fraction using relation (3), where the mass density of chitosan and graphene were replaced by epoxy resin $\rho_{EP} = 1.2$ g.cm^{-3} [63] and graphene oxide $\rho_{GO} = 2$ g.cm^{-3} [64], respectively. Figure 12b presents the experimentally measured thermal conductivity of the graphene oxide-epoxy composite from the works of Zhang *et al.* [59] and Zhang *et al.* [60], alongside the predicted values by our model at the microscale in two cases as the exfoliated structure and the intercalated structure (5 layers per block).

One may state that the results of the two experimental works are different, where Zhang *et al.* [60] obtained composites with higher thermal conductivity per graphene oxide content than those elaborated by Zhang *et al.* [59]. This may be due to the different dispersion of graphene oxide sheets in these two composites, which has not been described in detail in the two cited works. Indeed, in order to get comprehensive information on the microstructural morphology of the composite or the distribution of graphene oxide sheets, observations must be made at the nanoscale and in many different regions. Consequently, this information is usually not reported in detail in experimental works that do not focus on it. However, one can confirm that the three morphologies can be obtained for the composites upon dispersion of graphene oxide in the polymer matrix, namely the exfoliated structure, the intercalated structure and the partially exfoliated structure (which is the co-existence of the two previous structures) [23]. For $f_w < 5\%$, the models of exfoliated structure and intercalated structure, corresponding to the upper and lower bounds, may envelop the experimental results, implying the validity of the proposed model. On the other

hand, there were difficulties to generate RVEs containing more than 3% graphene oxide volume fraction (corresponding to $f_w > 5\%$) for the exfoliated structure. This issue arose due to the random orientation of the inclusions, leading to the lack of intersections between them; as a result, the monolayered graphene oxide sheets characterized with high aspect ratio became entangled preventing the creation of RVEs with a large graphene oxide volume fraction. Hbaieb *et al.* [58] encounters the same difficulty in creating clay inclusions with an aspect ratio of 50 for a clay volume fraction greater than 5%. In this study, the volume fraction of monolayer graphene oxide sheets that can be generated is limited to about 3% due to its larger aspect ratio of 67. In summary, our numerical model at the microscale is suitable for estimating the thermal conductivity of graphene oxide-polymer composites at the filler volume fraction from 0 to 3%.

5.3. Effective thermal conductivity of composite aerogels at the macroscale

After validating the model and performing simulations at the microscale, we transitioned to the macro scale by introducing these results into the model. At this scale, we investigated studies on the influence of structural parameters, including porosity, morphology, and presence of nanopores on the thermal conductivity of the aerogel. Additionally, a comparison with experimental data from the literature was also performed to validate the model.

5.3.1. Effect of porosity

Here, we investigated the effect of porosity on the thermal conductivity of aerogels while concurrently establishing a comparison between these numerical results and experimental measurements extracted from the literature. To mitigate the influences arising from the fillers (such as their distribution and intrinsic thermal conductivity, etc.), which are difficult to precisely control through experimental techniques, the thermal conductivity measurements obtained from pure polymer aerogels [65, 10, 11, 12, 13] were selected as the reference systems. Hence, the model employed here features a filler volume fraction of $f_v = 0\%$, meaning that the solid phase only consists of the polymer matrix with a thermal conductivity of $k_m = 0.2$ W/(m·K). The porosity of aerogel is considered in the range of 90-99.6%. With the purpose of verifying the model's robustness, we present here the predicted effective thermal conductivity by our model for two cases: one without nanopores and the other considering their presence.

In the first case, the aerogel is considered to have only micrometric pores. In the second case, there are 12% nanometric pores and 88% micrometric pores combined in the total pore volume of the aerogel. It is noteworthy that the terms "nanopores" and "macropores" used in this work, respectively to refer to the nanometric and micrometric pores. The thermal conductivity of the air confined in nanopores, which is significantly smaller than that of the free air, may be calculated using relation (30). Detailed procedures for calculating the effective thermal conductivity of aerogel while taking into account effect of nanopores will be provided in subsection 5.3.3.

Figure 13 shows the thermal conductivity estimated by our numerical model and the experimentally measured thermal conductivity of polyimide (PI) aerogel [10], chitosan (CS) aerogel [66], and cellulose nanofibril (CNF)-emulsion aerogel [9]. It should be noted that the nonzero components (i.e. diagonal components) of the effective thermal conductivity tensor at the macroscale $\mathbf{K}^{(3)}$ are the same due to the isotropic properties of solid phase and the symmetry of the hollow spherical unit cell.

From the numerical results, it can be observed that the effective thermal conductivity decreases as the porosity increases. At the same porosity, aerogels with 12% nanopore always have a lower thermal conductivity than aerogels composed only of macropores (0% nanopore). Furthermore,

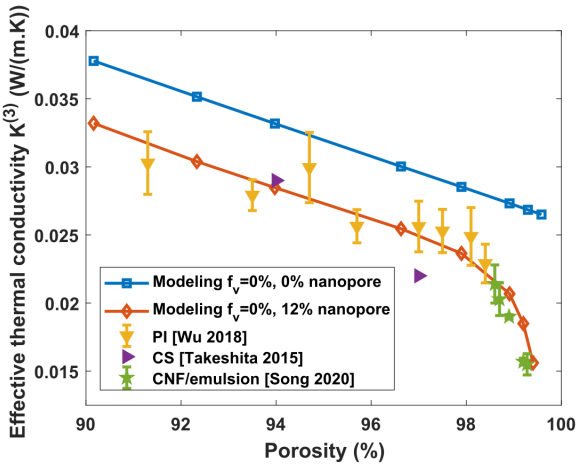

Figure 13: Numerical predictions of the effective thermal conductivity at the macroscale compared to the experimental data of polymer-based aerogel from literature [10, 66, 9].

a linear relationship between the effective thermal conductivity and porosity for the case of 0% nanopore can also be seen in the figure. On the contrary, this relationship becomes strongly non-linear in the case of 12% nanopore when the porosity is higher than 96%. This phenomenon is correlated with the Knudsen effect within nanopores [67], causing a reduction in the effective thermal conductivity of the aerogel below the free air thermal conductivity of 0.026 W/(m·K) when the porosity exceeds 96%. This effect will be discussed in more detail in subsection 5.3.3.

In relation to porosity, various methods can be employed to control the porosity of aerogels. Specifically, the referenced experimental works have reported that porosity can be influenced by factors such as crosslinking [10, 66], polymer concentration [10, 66] and emulsion templating [9], where the effect of polymer concentration is found to be the most significant. Accordingly, the porosity of aerogels can rise from 91.3 to 98.1% with a decrease in polyimide concentration from 10 to 1.1% (by weight), as previously reported [10], and from 86 to 97% with a corresponding decrease in chitosan concentration from 1.6 to 0.4% (by weight), as described elsewhere [66]. Therefore, the simulation results suggest that in order to reduce the effective thermal conductivity and enhance the insulation performance of the aerogel, it is advisable to decrease the polymer concentration.

The comparison between simulation results and experimental data indicates that the model of 0% nanopore overestimate the experimental data in most cases. This phenomenon can be explained by the fact that this case does not account for the impact of nanopores on the thermal conductivity of aerogels. Indeed, all three referenced experimental works report the existence of nanopores with diameters ranging from 3 to 50 nm. Besides, the results of the model with 12% nanopores match well with the experimental ones. This result suggests the significant influence of nanopores on the effective thermal conductivity of aerogels, which will be further investigated in detail in the following section. It is noted that the volume fraction of nanopores relative to the total pore volume has not been reported in these experimental works, thus only qualitative comparisons could be conducted and further investigations are needed. However, these results have also, to some extent, showcased the reliability of the proposed model for predicting the effective thermal conductivity of aerogels.

5.3.2. Effect of microstructural morphology

To investigate the effect of the structural parameters on the effective thermal conductivity of aerogels, the porosity was fixed at 98.24%, corresponding to the computed average value in subsection 3.1.3. As presented in subsection 3.1.1, 3 structures were considered, including graphene block with 5 layers per block (aggregate structure), monolayer graphene oxide (exfoliated structure) and graphene oxide block with 3 or 5 layers per block (intercalated structure). The volume fraction of the fillers (graphene and graphene oxide) was examined in the range of $0\% - 3\%$. Here, the estimated effective thermal conductivity at the macroscale has been normalized by the effective thermal conductivity of the pure polymer aerogel (*i.e.* $f_v = 0$) for ease of observation. The effective thermal conductivity tensor of this pure polymer aerogel is denoted by $\mathbf{K}_0^{(3)}$.

Figure 14a illustrates the normalized effective thermal conductivity at the macroscale as a function of the filler volume fraction for different structure types. It is evident that the effective thermal conductivity of aerogels increases as the volume fraction of the fillers rises. However, the extent of this increase varies among the different structural types. Specifically, graphene block contributes to the highest increase in thermal conductivity, followed by graphene oxide monolayer, and finally, graphene oxide blocks. It's interesting to consider that, at the macroscale, graphene oxide monolayer, graphene oxide blocks with 3 layers and graphene oxide block with 5 layers, only increases the effective thermal conductivity of aerogel by 6.4%, 3.6% and 2.8%, respectively, when the graphene oxide volume fraction is 3%. Meanwhile, these increments are recorded as 82%, 45%, and 35% at the microscale, as elucidated in subsection 5.2.2. It is noteworthy that in this study, the effective thermal conductivity at the micro- and macroscales respectively characterize the effective thermal conductivity of the composite (with extremely little to no pores) and the aerogel (ultraporous). These results provide a response to the question posed in subsection 5.2.2, indicating that graphene oxide can significantly enhance the thermal conductivity of polymer-based composites, while it does not substantially alter the thermal conductivity of polymer-based aerogels. This implies that graphene oxide can be employed flexibly for various applications.

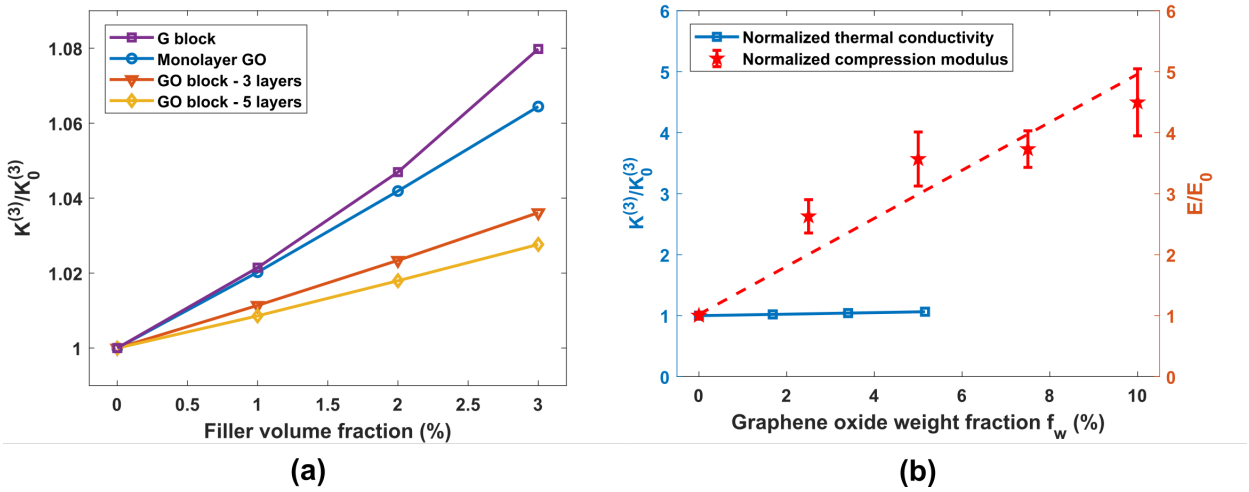

Figure 14: (a) Effect of the inclusion type-related structural parameter on the effective thermal conductivity of aerogel at the macroscale with a porosity of 98.24% and (b) estimated effective thermal conductivity by simulation and compressive modulus by experimentally measured as a function of graphene oxide weight fraction. The red dashed line represents to the line fitted by linear regression of the compressive modulus.

Regarding the comparison between graphene and graphene oxide, as observed in Fig. 14a, the polymer aerogel reinforced with graphene (aggregate structure) exhibits slightly higher thermal conductivity than that reinforced with graphene oxide (exfoliated structure). However, the results of the compression test demonstrate that graphene oxide exhibits a better capability for reinforcing mechanical properties compared to graphene (see Fig. 4). This result can be explained by the fact that, at high degree of oxidation, graphene oxide has a significantly lower thermal conductivity of about 1% compared to graphene [47], while its Young's modulus is only about 50% lower than that of graphene [68]. Furthermore, thanks to its functional groups on the surface, graphene oxide exhibits a strong dispersibility and may form covalent bonds with polymers, contributing to the enhancement of the mechanical properties of the aerogels.

In order to understand the impact of graphene oxide on the thermal conductivity and mechanical properties of the aerogels, we simultaneously represented both the effective thermal conductivity estimated by simulations and the compressive modulus that is experimentally measured as a function of graphene oxide weight fraction f_w (see Fig. 14b). It is noteworthy that both quantities were normalized by the effective thermal conductivity and compressive modulus of pure polymer aerogel ($f_w = 0$), respectively. The graphene oxide volume fraction f_v can be transformed into graphene oxide weight fraction f_w using Eq. (3). Figure 14b clearly illustrates that the compressive modulus increases with the weight fraction of graphene oxide, while the thermal conductivity remains nearly unchanged. Specifically, by employing linear regression on experimental results, the linear relationship obtained between compressive modulus and graphene oxide weight fraction indicates that the compressive modulus increases by 39% for each 1% weight fraction of graphene oxide added. Meanwhile, the rate of increase in effective thermal conductivity is only 1% for every 1% weight fraction of graphene oxide added. Furthermore, aerogels with an exfoliated structure of graphene oxide also exhibit more favorable characteristics compared to aerogels with an aggregate structure of graphene, such as improved thermal insulation and enhanced mechanical strength.

Based on the results of this section, it can be highlighted that the addition of graphene oxide significantly enhances the mechanical properties and reasonably increases the thermal conductivity of polymer-based aerogels. In the context where monolayer graphene sheets are prohibitively expensive and challenging to manufacture [69], monolayer graphene oxide, which can be readily produced on a massive scale at a reasonable cost, emerges as a promising candidate for reinforcing polymer-based aerogels.

5.3.3. Effect of nanopores occurrence

As discussed in subsection 5.3.1, porosity and presence of nanopores to various degrees are two critical factors that significantly affect the thermal conductivity of aerogels. Nevertheless, it should be noted that increasing the porosity to enhance thermal insulation performance also reduces the mechanical properties of the material, which should be taken into account in construction applications. Therefore, nanopore occurrence has, to be considered when developing porous materials with excellent thermal insulation while maintaining high rigidity. Indeed, with the same porosity, nanoporous materials possess lower thermal conductivity than common porous materials thanks to the extremely low gas thermal conductivity in the nanopores through the Knudsen effect [70]. This effect occurs when the mean free path (MFP) of the gas molecules is larger than the pore diameter, meaning that the gas molecules collide with the pore wall more frequently than with other gas molecules. As a result, the thermal conductivity of the gas becomes lower than the value for free gas. The gas thermal conductivity, denoted by k_g, taking into account the Knudsen effect, can be

written as follows [71]:

$$k_g = \frac{k_g^0}{1 + 2\beta\, \ell_m / D}, \tag{30}$$

where k_g^0 is the thermal conductivity of the free gas, $\mathrm{K}_n = \ell_m / D$ is the Knudsen number in which ℓ_m is the MFP of gas molecules and D is the characteristic size of pores, β is a coefficient varying between 1.5 and 2.0 characterizing the molecule-wall collision energy transfer efficiency (~ 2 for air). The quantity ℓ_m has been simply expressed by Stewart and Leiser as a function of temperature and pressure [72] as follows:

$$\ell_m = 2.303 \times 10^{-8} \times \frac{T}{P_g}, \quad \text{(cm)} \tag{31}$$

where T is the temperature and P_g is the gas pressure. From Eq. (31), it can be calculated that the MFP of gas molecules at room conditions ($T = 293$ K, $P_g = 1$ atm) is 67 nm. Therefore, an important impact of the Knudsen effect can be predicted for pores smaller than 67 nm in diameter.

In fact, nanopores and macropores coexist in the majority of aerogels, with sizes ranging from 1 to 50 nm and from a few micrometers to several hundreds of micrometers, respectively [73, 74, 75]. Additionally, the contribution of nanopores to the total pore volume is much lower than that of macropores, specifically ranging from 4 to 22%, as reported in previous studies [73, 74]. Hence, this study investigates the influence of nanopores on the overall thermal conductivity of aerogels from two aspects: (i) nanopore size and (ii) nanopore volume fraction. Here, due to the negligible impact of the Knudsen effect on the macropores, their diameter will be fixed at 76 μm. To accomplish this, the multiscale homogenization procedure introduced in section 4 requires an additional step. This step is employed at the nanoscale to calculate the effective thermal conductivity of the equivalent polymer matrix, where the spherical nanopores are regularly arranged within the polymer matrix. At this scale, the thermal conductivity of the gas phase within the nanopores, calculated by Eq. (30) and the thermal conductivity of the polymer matrix $k_p = 0.2$ W/(m·K) will be used for the homogenization issue. It should be noted that graphene oxide monolayer with a thermal conductivity $k_{GO} = 18$ W/(m·K) has been taken as a reference case; therefore, it is unnecessary to compute the effective thermal conductivity of the inclusion at the nanoscale. Next, the thermal conductivity of the equivalent homogenized matrix is used as input properties of the matrix at the microscale, and the homogenization process at both the micro- and macroscales is conducted as described in subsection 4.2. Furthermore, aerogels maintaining a total porosity of 98.24% and 2% volume fraction of graphene oxide monolayer are used throughout the studies in this section.

Figure 15 shows the pore size versus air thermal conductivity relationship at room conditions where $1 - 50$ nm is the range of the pore size investigation. It is clear that the thermal conductivity of the confined air decreases from 0.0042 W/(m·K) to 0.0001 W/(m·K) as the pore size decreases from 50 nm to 1 nm, and it is much smaller than that of free air (0.026 W/(m·K)). Next, the influence of pore size on the effective thermal conductivity of aerogel with 2% and 12% nanopore volume fractions is illustrated in Fig. 16a. It can be observed that a reduction in pore size leads to a decrease in the effective thermal conductivity of the aerogel, and this effect becomes more significant at higher nanopore volume fractions. The effective thermal conductivity in the case of 2% nanopore volume fraction appears to remain nearly constant, decreasing by 0.4% when the nanopore size decreases from 50 to 1 nm, whereas the case of 12% nanopore volume fraction records a reduction of 5.4%. This implies that enhancing the thermal insulation of the aerogel by reducing

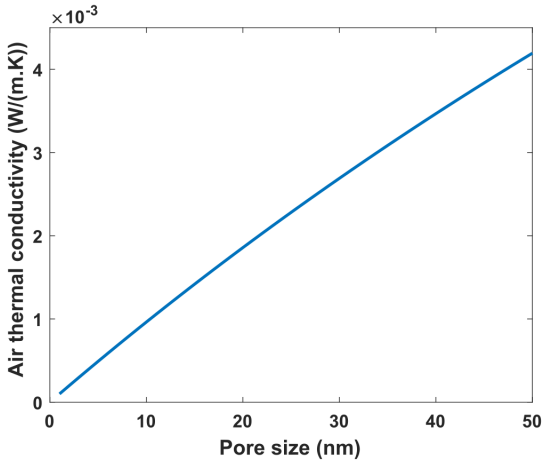

Figure 15: Air thermal conductivity as a function of the pore size at room condition.

the nanopore size is only significant when a substantial nanopore volume fraction is present within the aerogel. Furthermore, it is noteworthy that the volume fraction of nanopores has a significantly more pronounced impact on the effective thermal conductivity of the aerogel than the nanopore size. Indeed, at nanopore size of 1 nm, the thermal conductivity of the aerogels in the case of 12% nanopore volume fraction is 0.023 W/(m·K), decreasing by 20% compared to 0.027 W/(m·K) of the case of 2% nanopore volume fraction. To investigate the effect of nanopore volume fraction on the effective thermal conductivity of aerogel, we fixed the nanopore size at 4 nm and varied the nanopore volume fraction from 0 to 22% (see Fig. 16b).

One can observe that as the nanopore volume fraction increases from 0 to 22%, the effective thermal conductivity of aerogel decreases from 0.030 W/(m·K) to 0.017 W/(m·K), indicating a 43% of reduction. Moreover, a weak nonlinear relationship between the effective thermal conductivity and nanopore volume fraction can also be found. The influence of nanopore volume fraction diminishes slightly as the effective thermal conductivity approaches the value of 0.026 W/(m·K), which is free air thermal conductivity. Beyond this threshold, the effective thermal conductivity continues to decrease significantly as the nanopore volume fraction increases.

In fact, the nanopore volume within aerogels can be increased through various techniques. For instance, aerogels prepared by pyrolysis of resorcinol–furfural (RF) gel containing salt ($ZnCl_2$) will contain numerous nanopores as $ZnCl_2$ is removed [76]. Furthermore, cross-linkers can be employed to enhance the stability of the three-dimensional network structure, limiting the continuous growth of ice crystals during the freezing process, which results in the reduction in pore size of the aerogel [77]. It has also been demonstrated that the incorporation of graphene oxide into the polymer matrix creates favorable conditions for the formation of nanopores within the aerogel [7]. The numerical results in this section provide motivation for enhancing the thermal insulation performance of aerogels by increasing the volume of nanopores. Furthermore, in conjunction with the findings in subsection 5.3.2, it can be inferred that incorporating graphene oxide into polymer-based aerogels not only enhances their stiffness but also reduces their thermal conductivity, as the number of nanopores in the aerogel increases.

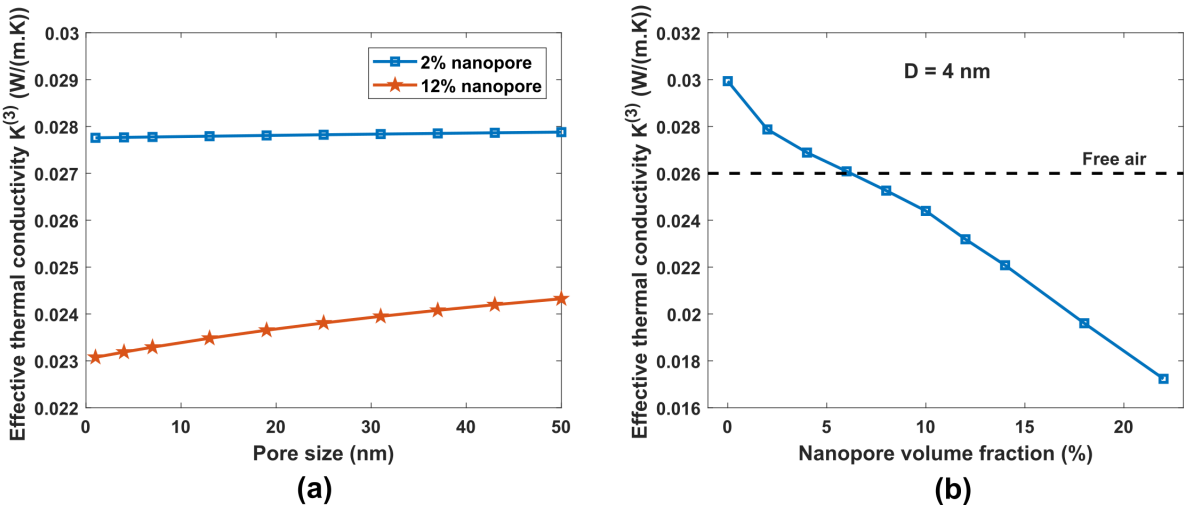

Figure 16: Effect of two parameters on effective thermal conductivity of aerogels at porosity of 98.24% and 2% graphene oxide volume fraction: (a) pore size with different volume fractions of nanopores, (b) nanopore volume fraction with pore size of 4 nm.

5.3.4. Effect of gas pressure

Gas pressure P_g has an important influence on the thermal conductivity of air. As the pressure decreases, the mean free path of the gas molecules l_m increases, leading to an increase in the impact of the Knudsen effect and thus a decrease in the gas thermal conductivity. The relationship between P_g and ℓ_m has been shown in Eq. (31). It can be deduced that during a decrease in gas pressure, the gas thermal conductivity is virtually unaffected until the MFP of gas molecules reaches values in the same order of size as the pore size. Therefore, the effect of gas pressure on the thermal conductivity of gas within smaller pores occurs earlier than in the case of gas within larger pores. Figure 17a illustrates the thermal conductivity of air contained within two types of pores of different sizes, including macropore ($D = 76$ μm) and nanopores ($D = 4$ nm), as a function of gas pressure in the range of $10^{-5} - 10$ atm. It is easy to see that the thermal conductivity of the air in the macropores is equal to that of the free air ($\sim$0.026 W/(m·K)), in other words there is no Knudsen effect. Its value decreases sharply when the gas pressure begins to decreases below 0.01 atm and approaches zero at vacuum pressure. Meanwhile, the thermal conductivity of the air in the nanopores was almost zero at room conditions ($P_g = 1$ atm), indicating that the effect of gas pressure has already occurred due to the small diameter of the nanopores.

In order to investigate the effect of gas pressure on the effective thermal conductivity of aerogel, we varied the gas pressure within the pores of aerogel from 10^{-5} to 10 atm. Here, aerogels have a constant porosity 98.24% and 2% graphene oxide volume fraction, with various cases of nanopore volume fractions considered. Figure 17b shows the variation of the effective thermal conductivity with respect to gas pressure for 3 cases of nanopore volume fractions, *i.e.* 0%, 6% and 12%. It is easy to see that the effective thermal conductivity decreases as the gas pressure decreases, following the same trend in all 3 cases. This effect becomes noticeable only when the pressure drops below 10^{-2} atm. Specifically, the thermal conductivity of aerogel can reach the values of 0.0025 W/(m·K), 0.0012 W/(m·K) and 0.0009 W/(m·K) at a pressure of 10^{-5} atm, respectively, for the cases of 0%, 2% and 3% nanopore volume fraction. Moreover, one can also observe that aerogels with large nanopore volume always have lower thermal conductivity at the same pressure. In other words,

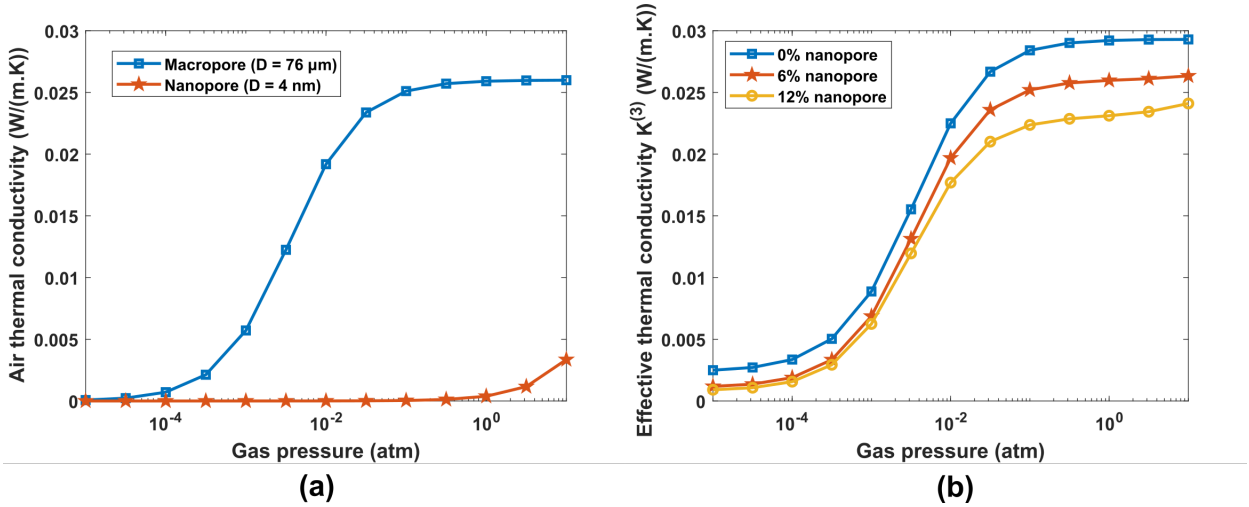

Figure 17: Effect of air pressure on (a) air thermal conductivity in nanopore with a diameter of 4 nm and in macropore with a diameter of 76 μm, and on (b) the thermal conductivity of aerogels at porosity of 98.24% and 2% graphene oxide volume fraction with different volume fractions of nanopores.

to achieve the same insulation performance, aerogels with a large nanopore volume need lower gas pressure than vacuum pressure. In essence, this is a compromise between the vacuum requirement and the nanopore volume to achieve optimal thermal insulation performances of porous materials. Indeed, it has been reported that VIPs cannot maintain a low inner pressure for a long period [3]. This suggests that the incorporation of aerogel as the core material for VIPs to achieve optimal insulation performance could be a promising solution to this problem. It should also be noted that the core material in VIPs needs to possess sufficient mechanical properties to withstand the pressure of the envelope without collapsing. One can increase the mass density of aerogel, meaning reduce porosity, to ensure a certain mechanical strength, although solid phase conduction increases. However, with the Knudsen effect in nanopores and the low gas pressure, the effective thermal conductivity of the porous material can be decreased. This is a multifaced issue involving a delicate compromise between three factors, namely: mechanical strength, nanopore volume fraction, and gas pressure, all of which requires further research.

6. Conclusion

This work employed a multiscale approach for the numerical characterizations of the effective thermal conductivity of polymer aerogels reinforced by graphene and graphene oxide. This composite aerogel type has gained tremendous attention due to its environmentally friendly manufacturing process, which combines the use of biopolymers and freeze-drying techniques. In the proposed multiscale approach to characterize the effective thermal properties of the studied aerogels, geometrical configurations were constructed at three scales, referred to as nano-, micro-, and macroscales, based on experimental characterization. Subsequently, the homogenization process was conducted from smaller to larger scales, wherein Milton's method was employed at the nanoscale, and the asymptotic homogenization method combined with the finite element method was utilized at the micro- and macroscales. Three types of inclusions forms related to the aggregate structure of graphene, exfoliated and intercalated structures of graphene oxide were investigated. By randomly generating

these inclusions in the polymer matrix at the microscale and employing a hollow spherical representative unit cell at the macroscale, the relationship was established between the effective thermal conductivity of the aerogel and microstructure characteristics, namely microstructural morphology, porosity, pore size, as well as gas pressure.

Comparisons between simulation results and experimental data validated the accuracy of the proposed model. It was shown that the addition of graphene and graphene oxide did not significantly alter the effective thermal conductivity of the aerogel while notably enhancing its mechanical properties. The numerical results demonstrated that the exfoliated structure of graphene oxide offered the most beneficial application for enhancing the stiffness of the polymer aerogel and ensuring a reasonable increase in thermal conductivity compared to other structures. The numerical results also suggested that reducing the polymer concentration in the precursor solution increased the porosity of the aerogel, leading to a decrease in its effective thermal conductivity. Furthermore, the thermal insulation performance of the materials could be significantly enhanced by reducing the pore size to below 50 nm, or in other words, increasing the number of these nanopores through the introduction of cross-linkers or the increase in the graphene oxide content. In relation to the effect of gas pressure, it was demonstrated that reducing the gas pressure below 10^{-2} atm significantly decreased the effective thermal conductivity of the aerogels, and concurrently, aerogels with numerous nanopores required less vacuum demand for the same thermal insulation performance. Based on these numerical results, it is suggested to integrate aerogels as the core material of vacuum insulation panels to achieve optimal thermal insulation performance while ensuring that the aerogels are sufficiently rigid to withstand the pressure of the envelope without collapsing.

To obtain initial estimates of the effective thermal properties of the studied aerogels, the multiscale approach herein focusing on the ideal disc-shaped of graphene and graphene oxide has proven to be useful in the material development phase. Nonetheless, graphene and graphene oxide predominantly exhibit defects in their two-dimensional structures, such as the out-of-plane wrinkles and hole defects [78]. These factors may provide deeper insights into the effects of graphene and graphene oxide on the effective thermal properties of polymer-based materials, which will be the topic of a further investigation. Additionally, the proposed integration of aerogels with nanopores as cores for VIPs demands more in-depth research on both experimental and simulation aspects. This constitutes a complex challenge in finding a compromise between three key factors, *i.e.* thermal conductivity, gas pressure, and mechanical properties. Specifically, experimental work must provide sufficient data on the stiffness, porosity, and corresponding volume fraction of nanopores, while simulation work will estimate the effective thermal conductivity of these materials under varying gas pressure conditions. With the target insulation performance corresponding to a specific gas pressure, the optimal material will be suitable for application as a core material provided its stiffness is adequat to withstand the pressure exerted by the envelope at this pressure level.

Acknowledgements

This work has benefited from a French government grant managed by ANR within the frame of the national program of Investments for the Future ANR-11-LABX-0022-01 (LabEx MMCD project).

References

[1] L. Chen, Y. Zhao, R. Xie, B. Su, Y. Liu, X. Renfei, Embodied energy intensity of global high energy consumption industries: A case study of the construction industry, Energy 277 (2023) 127628.

[2] M. González-Torres, L. Pérez-Lombard, J. Coronel, I. Maestre, D. Yan, A review on buildings energy information: Trends, end-uses, fuels and drivers, Energy Reports 8 (2022) 626–637. doi:https://doi.org/10.1016/j.egyr.2021.11.280.
URL https://www.sciencedirect.com/science/article/pii/S235248472101427X

[3] M. Alam, H. Singh, M. Limbachiya, Vacuum insulation panels (vips) for building construction industry – a review of the contemporary developments and future directions, Applied Energy 88 (11) (2011) 3592–3602. doi:https://doi.org/10.1016/j.apenergy.2011.04.040.
URL https://www.sciencedirect.com/science/article/pii/S0306261911002753

[4] M. Hasan, R. Sangashetty, A. Esther, S. Patil, B. Sherikar, A. Dey, Prospect of thermal insulation by silica aerogel: a brief review, Journal of The Institution of Engineers (India): Series D 98 (2017) 297–304.

[5] X. Ge, Y. Shan, L. Wu, X. Mu, H. Peng, Y. Jiang, High-strength and morphology-controlled aerogel based on carboxymethyl cellulose and graphene oxide, Carbohydrate polymers 197 (2018) 277–283.

[6] M. de Luna, C. Ascione, C. Santillo, L. Verdolotti, M. Lavorgna, G. Buonocore, R. Castaldo, G. Filippone, H. Xia, L. Ambrosio, Optimization of dye adsorption capacity and mechanical strength of chitosan aerogels through crosslinking strategy and graphene oxide addition, Carbohydrate polymers 211 (2019) 195–203.

[7] M. Sarno, L. Baldino, C. Scudieri, S. Cardea, P. Ciambelli, E. Reverchon, Sc-co2-assisted process for a high energy density aerogel supercapacitor: the effect of go loading, Nanotechnology 28 (20) (2017) 204001. doi:10.1088/1361-6528/aa67d9.
URL https://dx.doi.org/10.1088/1361-6528/aa67d9

[8] C. Simón-Herrero, S. Caminero-Huertas, A. Romero, J. Valverde, L. Sánchez-Silva, Effects of freeze-drying conditions on aerogel properties, Journal of Materials Science 51 (2016) 8977–8985.

[9] M. Song, J. Jiang, H. Qin, X. Ren, F. Jiang, Flexible and super thermal insulating cellulose nanofibril/emulsion composite aerogel with quasi-closed pores, ACS Applied Materials & Interfaces 12 (40) (2020) 45363–45372, pMID: 32931232. arXiv:https://doi.org/10.1021/acsami.0c14091, doi:10.1021/acsami.0c14091.
URL https://doi.org/10.1021/acsami.0c14091

[10] Y.-W. Wu, W.-C. Zhang, R.-J. Yang, Ultralight and low thermal conductivity polyimide–polyhedral oligomeric silsesquioxanes aerogels, Macromolecular Materials and Engineering 303 (2) (2018) 1700403.

[11] Z. Fu, J. Corker, T. Papathanasiou, Y. Wang, Y. Zhou, O. Madyan, F. Liao, M. Fan, Critical review on the thermal conductivity modelling of silica aerogel composites, Journal of Building Engineering 57 (2022) 104814.

[12] B. Goodarzi, A. Bahramian, Applying machine learning for predicting thermal conductivity coefficient of polymeric aerogels, Journal of Thermal Analysis and Calorimetry 147 (2022) 6227–6238.

[13] F. He, Y. Wang, W. Zheng, J.-Y. Wu, Y.-H. Huang, Effective thermal conductivity model of aerogel thermal insulation composite, International Journal of Thermal Sciences 179 (2022) 107654.

[14] S. Zeng, A. Hunt, R. Greif, Geometric structure and thermal conductivity of porous medium silica aerogel, Journal of Heat Transfer 117 (4) (1995) 1055–1058.

[15] D. Dan, H. Zhang, W.-Q. Tao, Effective structure of aerogels and decomposed contributions of its thermal conductivity, Applied Thermal Engineering 72 (1) (2014) 2–9, aSCHT2013. doi:https://doi.org/10.1016/j.applthermaleng.2014.02.052.
URL https://www.sciencedirect.com/science/article/pii/S1359431114001446

[16] T. Xie, Y.-L. He, Z.-J. Hu, Theoretical study on thermal conductivities of silica aerogel composite insulating material, International Journal of Heat and Mass Transfer 58 (1) (2013) 540–552. doi:https://doi.org/10.1016/j.ijheatmasstransfer.2012.11.016.
URL https://www.sciencedirect.com/science/article/pii/S001793101200871X

[17] J.-L. Auriault, C. Boutin, C. Geindreau, Homogenization of coupled phenomena in heterogenous media, Hermes Science Publications, 2009.

[18] V.-S. Vo, S. Mahouche-Chergui, V.-H. Nguyen, S. Naili, N. Singha, B. Carbonnier, Chapter 5 - chemical and photochemical routes toward tailor-made polymer–clay nanocomposites: Recent progress and future prospects, in: K. Jlassi, M. M. Chehimi, S. Thomas (Eds.), Clay-Polymer Nanocomposites, Elsevier, 2017, pp. 145–197.

[19] V.-S. Vo, S. Mahouche-Chergui, V.-H. Nguyen, S. Naili, B. Carbonnier, Crucial role of covalent surface functionalization of clay nanofillers on improvement of the mechanical properties of bioepoxy resin, ACS Sustainable Chemistry & Engineering 7 (18) (2019) 15211–15220.

[20] W. Gul, S. Akbar Shah, A. Khan, N. Ahmad, S. Ahmed, N. Ain, A. Mehmood, B. Salah, S. Ullah, R. Khan, Synthesis of graphene oxide (go) and reduced graphene oxide (rgo) and their application as nano-fillers to improve the physical and mechanical properties of medium density fiberboard, Front. Mater. 10 (2023) 1206918.

[21] X. Fu, J. Lin, Z. Liang, R. Yao, W. Wu, Z. Fang, W. Zou, Z. Wu, H. Ning, J. Peng, Graphene oxide as a promising nanofiller for polymer composite, Surfaces and Interfaces 37 (2023) 102747.

[22] D.-T. Le, B. Carbonnier, S. Hamadi, D. Grande, M. Fois, S. Naili, S. Nguyen, V.-H.and Mahouche-Chergui, Toward the development of graphene/chitosan biocomposite aerogels with enhanced mechanical and thermal insulation performance, ACS Appl. Polym. Mater. 6 (2024) 13132–13146.

[23] J. Jang, M. Kim, H. Jeong, C. Shin, Graphite oxide/poly (methyl methacrylate) nanocomposites prepared by a novel method utilizing macroazoinitiator, Composites Science and Technology 69 (2) (2009) 186–191.

[24] T. Blanton, D. Majumdar, X-ray diffraction characterization of polymer intercalated graphite oxide, Powder Diffraction 27 (2) (2012) 104–107.

[25] B. Tan, N. Thomas, A review of the water barrier properties of polymer/clay and polymer/graphene nanocomposites, Journal of Membrane Science 514 (2016) 595–612. doi:https://doi.org/10.1016/j.memsci.2016.05.026.
URL https://www.sciencedirect.com/science/article/pii/S0376738816303726

[26] L. Wang, J. Wang, L. Zheng, Z. Li, L. Wu, X. Wang, Superelastic, anticorrosive, and flame-resistant nitrogen-containing resorcinol formaldehyde/graphene oxide composite aerogels, ACS Sustainable Chemistry & Engineering 7 (12) (2019) 10873–10879.

[27] W. Sun, A. Du, G. Gao, J. Shen, G. Wu, Graphene-templated carbon aerogels combining with ultra-high electrical conductivity and ultra-low thermal conductivity, Microporous and Mesoporous Materials 253 (2017) 71–79.

[28] W. Van De Walle, H. Janssen, A 3D model to predict the influence of nanoscale pores or reduced gas pressures on the effective thermal conductivity of cellular porous building materials, Journal of Building Physics 43 (4) (2020) 277–300. arXiv:https://doi.org/10.1177/1744259119874489, doi:10.1177/1744259119874489.
URL https://doi.org/10.1177/1744259119874489

[29] Q.-B. Nguyen, V.-H. Nguyen, A. Rios de Anda, E. Renard, S. Naili, Multiscale characterization of effective thermal properties by an asymptotic homogenization method of a biosourced epoxy resin with two porosity levels, Archive of Applied Mechanics 91 (9) (2021) 3773–3797.

[30] X. Chen, Z. Qu, Z. Liu, G. Ren, Mechanism of oxidization of graphite to graphene oxide by the Hummers method, ACS Omega 7 (2022) 23503–23510.

[31] D. Klvana, J. Chaouki, M. Repellin-Lacroix, G. Pajonk, A new method of preparation of aerogel-like materials using a freeze-drying process, Le Journal de Physique Colloques 50 (C4) (1989) C4–29.

[32] I. Polyzos, M. Bianchi, L. Rizzi, E. Koukaras, J. Parthenios, K. Papagelis, R. Sordan, C. Galiotis, Suspended monolayer graphene under true uniaxial deformation, Nanoscale 7 (2015) 13033–13042. doi:10.1039/C5NR03072B.
URL http://dx.doi.org/10.1039/C5NR03072B

[33] I. Nikolaou, H. Hallil, V. Conédéra, B. Plano, O. Tamarin, J.-L. Lachaud, D. Talaga, S. Bonhommeau, C. Dejous, D. Rebière, Electro-mechanical properties of inkjet-printed graphene oxide nanosheets, physica status solidi (a) 214 (3) (2017) 1600492. arXiv:https://onlinelibrary.wiley.com/doi/pdf/10.1002/pssa.201600492, doi:https://doi.org/10.1002/pssa.201600492.
URL https://onlinelibrary.wiley.com/doi/abs/10.1002/pssa.201600492

[34] S. Wang, J. Pu, D. Chan, B. Cho, K. Loh, Wide memory window in graphene oxide charge storage nodes, Applied Physics Letters 96 (14) (2010) 143109.

[35] C. Wan, M. Frydrych, B. Chen, Strong and bioactive gelatin–graphene oxide nanocomposites, Soft Matter 7 (13) (2011) 6159–6166.

[36] B. Mortazavi, O. Benzerara, H. Meyer, J. Bardon, S. Ahzi, Combined molecular dynamics-finite element multiscale modeling of thermal conduction in graphene epoxy nanocomposites, Carbon 60 (2013) 356–365.

[37] R. Rafiee, A. Eskandariyun, Estimating Young's modulus of graphene/polymer composites using stochastic multi-scale modeling, Composites Part B: Engineering 173 (2019) 106842.

[38] V. Shevchenko, S. Polschikov, P. Nedorezova, A. Klyamkina, A. Shchegolikhin, A. Aladyshev, V. Muradyan, In situ polymerized poly (propylene)/graphene nanoplatelets nanocomposites: Dielectric and microwave properties, Polymer 53 (23) (2012) 5330–5335.

[39] S. Polschikov, P. Nedorezova, A. Klyamkina, A. Kovalchuk, A. Aladyshev, A. Shchegolikhin, V. Shevchenko, V. Muradyan, Composite materials of graphene nanoplatelets and polypropylene, prepared by in situ polymerization, Journal of Applied Polymer Science 127 (2) (2013) 904–911.

[40] X. Sun, Z. Liu, K. Welsher, J. Robinson, A. Goodwin, S. Zaric, H. Dai, Nano-graphene oxide for cellular imaging and drug delivery, Nano research 1 (3) (2008) 203–212.

[41] X. Zhang, X. Zhao, T. Xue, F. Yang, W. Fan, T. Liu, Bidirectional anisotropic polyimide/bacterial cellulose aerogels by freeze-drying for super-thermal insulation, Chemical Engineering Journal 385 (2020) 123963.

[42] S. Takeshita, A. Sadeghpour, W. Malfait, A. Konishi, K. Otake, S. Yoda, Formation of nanofibrous structure in

biopolymer aerogel during supercritical co2 processing: The case of chitosan aerogel, Biomacromolecules 20 (5) (2019) 2051–2057.
[43] J. Robertson, Properties of diamond-like carbon, Surface and Coatings Technology 50 (3) (1992) 185–203.
[44] C. Zhan, S. Jana, Shrinkage reduced polyimide-graphene oxide composite aerogel for oil absorption, Microporous and Mesoporous Materials 307 (2020) 110501.
[45] M. Pelaez-Fernandez, A. Bermejo, A. Benito, W. Maser, R. Arenal, Detailed thermal reduction analyses of graphene oxide via in-situ tem/eels studies, Carbon 178 (2021) 477–487.
[46] E. Pop, V. Varshney, A. Roy, Thermal properties of graphene: Fundamentals and applications, MRS bulletin 37 (12) (2012) 1273–1281.
[47] S. Lin, M. Buehler, Thermal transport in monolayer graphene oxide: Atomistic insights into phonon engineering through surface chemistry, Carbon 77 (2014) 351–359.
[48] N. Mahanta, A. Abramson, Thermal conductivity of graphene and graphene oxide nanoplatelets, in: 13th intersociety conference on thermal and thermomechanical phenomena in electronic systems, IEEE, 2012, pp. 1–6.
[49] X. Huang, P. Jiang, T. Tanaka, A review of dielectric polymer composites with high thermal conductivity, IEEE Electrical Insulation Magazine 27 (4) (2011) 8–16. doi:10.1109/MEI.2011.5954064.
[50] G. Milton, The theory of composites, Cambridge Monographs on Applied and Computational Mathematics, Cambridge University Press, 2002, Ch. Laminate materials, p. 159–184.
[51] C. Mei, B. Vernescu, Homogenization methods for multiscale mechanics, World scientific, 2010.
[52] Comsol Multiphysics, Comsol AB, Stockholm, Sweden (2019).
[53] E. Ghossein, M. Lévesque, Random generation of periodic hard ellipsoids based on molecular dynamics: A computationally-efficient algorithm, Journal of Computational Physics 253 (2013) 471–490.
[54] B. Lubachevsky, F. Stillinger, Geometric properties of random disk packings, Journal of Statistical Physics 60 (1990) 561–583.
[55] B. Widom, Random Sequential Addition of Hard Spheres to a Volume, The Journal of Chemical Physics 44 (10) (2004) 3888–3894.
[56] J. Feder, Random sequential adsorption, Journal of Theoretical Biology 87 (2) (1980) 237–254.
[57] B. Mortazavi, M. Baniassadi, J. Bardon, S. Ahzi, Modeling of two-phase random composite materials by finite element, Mori-Tanaka and strong contrast methods, Composites Part B: Engineering 45 (1) (2013) 1117–1125.
[58] K. Hbaieb, Q. Wang, Y. Chia, B. Cotterell, Modelling stiffness of polymer/clay nanocomposites, Polymer 48 (3) (2007) 901–909.
[59] L. Zhang, W. Zhu, Y. Huang, S. Qi, Synergetic effects of silver nanowires and graphene oxide on thermal conductivity of epoxy composites, Nanomaterials 9 (9) (2019) 1264.
[60] C. Zhang, T. Li, H. Song, Y. Han, Y. Dong, Y. Wang, Q. Wang, Improving the thermal conductivity and mechanical property of epoxy composites by introducing polyhedral oligomeric silsesquioxane-grafted graphene oxide, Polymer Composites 39 (S3) (2018) E1890–E1899.
[61] L. Hu, T. Desai, P. Keblinski, Thermal transport in graphene-based nanocomposite, Journal of Applied Physics 110 (3) (2011) 033517.
[62] K. Zarasvand, H. Golestanian, Investigating the effects of number and distribution of gnp layers on graphene reinforced polymer properties: Physical, numerical and micromechanical methods, Composites Science and Technology 139 (2017) 117–126.
[63] J. King, D. Klimek, I. Miskioglu, G. Odegard, Mechanical properties of graphene nanoplatelet/epoxy composites, Journal of Applied Polymer Science 128 (6) (2013) 4217–4223.
[64] M. Pelaez-Fernandez, A. Bermejo, A. Benito, W. Maser, R. Arenal, Detailed thermal reduction analyses of graphene oxide via in-situ tem/eels studies, Carbon 178 (2021) 477–487. doi:https://doi.org/10.1016/j.carbon.2021.03.018.
URL https://www.sciencedirect.com/science/article/pii/S0008622321003213
[65] T. Zhang, Y. Zhao, X. Ma, K. Wang, The effect of poor solvent on the microstructures and thermal insulation performance of polyimide aerogels, Materials Letters 300 (2021) 130151.
[66] S. Takeshita, S. Yoda, Chitosan aerogels: transparent, flexible thermal insulators, Chemistry of Materials 27 (22) (2015) 7569–7572.
[67] B. Merillas, J. Vareda, J. Martín-de León, M. Rodríguez-Pérez, L. Durães, Thermal conductivity of nanoporous materials: where is the limit?, Polymers 14 (13) (2022) 2556.
[68] L. Liu, J. Zhang, J. Zhao, F. Liu, Mechanical properties of graphene oxides, Nanoscale 4 (2012) 5910–5916. doi:10.1039/C2NR31164J.
URL http://dx.doi.org/10.1039/C2NR31164J

[69] N. Kumar, R. Salehiyan, V. Chauke, O. Joseph Botlhoko, K. Setshedi, M. Scriba, M. Masukume, S. Sinha Ray, Top-down synthesis of graphene: A comprehensive review, FlatChem 27 (2021) 100224. doi:https://doi.org/10.1016/j.flatc.2021.100224.
URL https://www.sciencedirect.com/science/article/pii/S2452262721000039

[70] B. Jelle, A. Gustavsen, R. Baetens, The path to the high performance thermal building insulation materials and solutions of tomorrow, Journal of Building Physics 34 (2) (2010) 99–123.

[71] M. Kaganer, Thermal insulation in cryogenic engineering, Israel Program for Scientific Translations, 1969.
URL https://cir.nii.ac.jp/crid/1130282270460464768

[72] D. Stewart, D. Leiser, Characterization of the thermal conductivity for fibrous refractory composite insulations, in: Proceedings of the 9th Annual Conference on Composites and Advanced Ceramic Materials: Ceramic Engineering and Science Proceedings, Vol. 6, Wiley Online Library, 1985, pp. 769–792.

[73] C. Daniel, B. Nagendra, M. Acocella, E. Cascone, G. Guerra, Nanoporous crystalline composite aerogels with reduced graphene oxide, Molecules 25 (22) (2020) 5241. doi:10.3390/molecules25225241.
URL http://dx.doi.org/10.3390/molecules25225241

[74] L. Daero, J. Kim, S. Kim, G. Kim, J. Roh, S. Lee, H. Han, Tunable pore size and porosity of spherical polyimide aerogel by introducing swelling method based on spherulitic formation mechanism, Microporous and Mesoporous Materials 288 (2019) 109546. doi:https://doi.org/10.1016/j.micromeso.2019.06.008.
URL https://www.sciencedirect.com/science/article/pii/S1387181119303890

[75] G. Horvat, M. Pantić, Ž. Knez, Z. Novak, A brief evaluation of pore structure determination for bioaerogels, Gels 8 (438) (2022) 1–18.

[76] H. Zhang, J. Feng, L. Li, Y. Jiang, J. Feng, Preparation of a carbon fibre-reinforced carbon aerogel and its application as a high-temperature thermal insulator, RSC Adv. 12 (2022) 13783–13791. doi:10.1039/D2RA00276K.
URL http://dx.doi.org/10.1039/D2RA00276K

[77] H.-B. Chen, B. Liu, W. Huang, J.-S. Wang, G. Zeng, W.-H. Wu, D. Schiraldi, Fabrication and properties of irradiation-cross-linked poly(vinyl alcohol)/clay aerogel composites, ACS Applied Materials & Interfaces 6 (18) (2014) 16227–16236, pMID: 25164075. arXiv:https://doi.org/10.1021/am504418w, doi:10.1021/am504418w.
URL https://doi.org/10.1021/am504418w

[78] B. Genorio, K. Harrison, J. Connell, G. Dražić, K. Zavadil, N. Markovic, D. Strmcnik, Tuning the selectivity and activity of electrochemical interfaces with defective graphene oxide and reduced graphene oxide, ACS Applied Materials & Interfaces 11 (37) (2019) 34517–34525, pMID: 31430112. arXiv:https://doi.org/10.1021/acsami.9b13391, doi:10.1021/acsami.9b13391.
URL https://doi.org/10.1021/acsami.9b13391